The Corrosion and Tensile Characteristics of Hot-Wire Deposited 316L Stainless-Steel: An Analysis of Four Printing Methods

by

Brandon Lee Koenig

Submitted in Partial Fulfillment of the Requirements

for the Degree of

Master of Science in Engineering

in

Chemical Engineering

YOUNGSTOWN STATE UNIVERSITY

August, 2024

The Corrosion and Tensile Characteristics of Hot-Wire Deposited 316L Stainless-Steel: An Analysis of Four Printing Methods

Brandon Lee Koenig

I hereby release this thesis to the public. I understand that this thesis will be made available from the OhioLINK ETD Center and the Maag Library Circulation Desk for public access. I also authorize the University or other individuals to make copies of this thesis as needed for scholarly research.

Signature:

_____

Brandon Koenig, Student Date

Approvals:

_____

Holly Martin, PhD, Thesis Advisor Date

_____

Pedro Cortes, PhD, Committee Member Date

_____

Bharat Yelamanchi, PhD, Committee Member Date

_____

Salvatore A. Sanders, PhD, Dean, College of Graduate Studies Date

ABSTRACT

A longitudinal study in corrosion was performed on tensile-elongation dog-bones, created using 3D-printed stainless steel. The effects of exposure to an acidic environment were investigated regarding mass-loss, tensile and yield strength, modulus of elasticity, profilometry of pits and defects, and microscopy of fracture-sites. The SS316L specimens were manufactured using different print-directions, specifically overlapping unidirectional or rotated bidirectional for each layer by an additive manufacturing unit, the Mazak VC-500/5X AM HWD.

The novel aspect of this research is focusing on the differences that the path the hot-wire, direct energy deposition, print-head has on its corrosion characteristics, as opposed to only focusing on the printing-parameters. The goal was to determine what printing-directions and methods were best for resisting corrosion.

The research outlines the process of preparing samples for controlled weight-loss in HCl as well as the methods used to measure the mechanical properties. This allows for the results to be repeated if desired.

Upon thoroughly reviewing the data and drawing connections where applicable, it was determined within the test samples that unidirectional print-directions yielded better mass-loss and mechanical attributes than bidirectional printing. It was found that some print directions, namely 90°, which is perpendicular to the printing door, performed notably better than other directions such as 0° or 45°.

Table of Contents

The Corrosion and Tensile Characteristics of Hot-Wire Deposited 316L Stainless-Steel: An Analysis of Four Printing Methods

The additive manufacturing of stainless-steel parts is a frequently discussed subject in the realm of material science and industry; this is due to the attractive physical properties of stainless-steel and the cost-savings and time-reduction versus conventional manufacturing methods such as casting and CNC machining. By utilizing additive manufacturing, parts are able to be custom-made without the use of molds and very little wasted material.

Corrosion properties of additively manufactured steel parts is a topic visited in research previously, but typically through short duration experiments where the samples are put under a constant load, or a current is being applied. It is important to analyze the effects of longer duration corrosion dwell times.

316L stainless-steel (SS) is an austenitic form of steel which has a lower carbon composition than regular SS316 [1]. Austenitic refers to the crystalline lattice structure of iron, specifically that of face-centered-cubic [2]. Shown below in Table 1 is the composition of various alloys of 300-series stainless steel including SS316L:

Table 1: Chemical Composition of Various 300-Series Stainless-Steel by %

Stainless Steel	C, ≤	Mn, ≤	P, ≤	S, ≤	Si, ≤	Cr	Ni	Mo
304	0.08	2.00	0.045	0.03	1.00	18.0-20.0	8.0-11.0	–
304L	0.03	2.00	0.045	0.03	1.00	18.0-20.0	8.0-12.0	–
316	0.08	2.00	0.045	0.030	1.00	16.0-18.0	10.0-14.0	2.00-3.00
316L	0.03	2.00	0.045	0.030	1.00	16.0-18.0	10.0-14.0	2.00-3.00

From Table 1, the composition that makes SS316L unique versus SS304 is the lower carbon concentration, higher nickel, slightly lower chromium, and the addition of molybdenum. For a more precise definition of the composition of SS316L or other chromium and chromium-nickel containing steels, reference the ASTM A240/A240M standard [3]. SS316 has a carbon concentration of 0.08% as opposed to SS316L's 0.03%. The lower carbon concentration and presence of molybdenum plays a role in avoiding chromium-carbide precipitation, or the formation of chromium and carbide complexes, that can occur during high temperature processes such as welding or hot-wire, Direct-Energy-Deposition (DED) of steel. For 316 Stainless Steel with a carbon concentration of 0.07%, this precipitation can occur at 800-1600°F [4].

SS316L is often used in applications where corrosion-resistance is desired, such as with marine-vessels and outdoor environments where there is an exposure to chlorides [5].

It is for this reason that it is important to verify whether additive manufacturing techniques significantly reduce the corrosion resistance of parts over long durations of exposure to corrosive environments causing it to perform below the standards of parts manufactured in a more conventional method. There are plenty of additional challenges that arise from additively manufactured steel, such as pores, inclusions, or lack of fusion that can occur as a result of an additive manufacturing process [6]. Localized compositional changes of the print-material can even occur due to the thermal process of melting steel wire.

Corrosion is defined as a reduction-oxidation (redox) reaction that converts the base material into a more electrochemically stable form. Corrosion, if not controlled, reduces the mechanical properties of materials and can result in the premature failure of a part that is placed under stress. Corrosion cannot be completely avoided in steel as the creation of iron-oxides is electrochemically spontaneous [7]. The added chromium in SS316L protects the surface of the

steel from forming iron-oxides as readily. This occurs by substituting a layer of iron-oxides with chromium-oxides, which are even more electrochemically spontaneous and stable, and do not flake off unlike iron-oxide. It thereby substantially reduces the mass-loss of iron, since the chromium-oxide layer is not actively being removed and leaching from the iron. This slows down the oxidation process of iron since atmospheric oxygen is no longer in direct contact with iron, and therefore, unable to easily form the iron-oxides [6].

Chromium-carbide precipitation, as mentioned previously offers a pathway for corrosion to occur readily in stainless-steels like SS316L. If the chromium has precipitated between the grains of the microstructure, the chromium-depleted regions are unable to replenish a passivated layer of chromium-oxide and therefore will form iron-oxides in localized regions. This results in intergranular corrosion that also weakens the material despite the presence of a chromium-oxide film. The phenomena of chromium-carbide precipitation can also be further reduced by using nitrogen-rich steels, which is where nitrogen exceeds 0.4% in austenitic steels [8].

Another pathway for corrosion in steel is that of hydrogen embrittlement. Hydrogen embrittlement is where monatomic hydrogen, produced by the release of hydrogen during the corrosion reactions absorbs into the metal interstitially at a stress-point in the material, such as a surface defect or a bend [9]. In the case of steel, ferrous hydrides are formed, which are known to be very unstable and brittle [10]. The build-up of molecular hydrogen immediately outside of the stress-point causes the embrittled surface to further crack, which then causes the process to continue. Hydrogen embrittlement is a process that happens most readily in high pressure, ambient temperature environments and typically, in lower nickel-containing steels [9]. However, it can happen in all environments where hydrogen is a by-product of the corrosion reaction, like equation 3 shown below, prior to the production of diatomic hydrogen.

Pitting corrosion can occur in environments where the steel is constantly exposed to corrosive media. In the case of steel immersed in a bath of HCl, a self-perpetuating cycle can proceed by the following equations:

$$FeO + 2HCl \rightarrow FeCl_2 + H_2O \quad (1)$$

$$FeCl_2 + 2H_2O \rightarrow Fe(OH)_2 + 2HCl \quad (2)$$

$$2Fe(OH)_2 + 2H_2O \rightarrow 2Fe(OH)_3 + H_2 \quad (3)$$

$$2Fe(OH)_3 \rightarrow Fe_2O_3 + 3H_2O \quad (4)$$

As seen in Equations 1 and 2, as iron-oxide is converted to ferrous-chloride and then ferrous-hydroxide, water is being converted to hydrochloric acid. Ferrous hydroxide is mostly insoluble in water and can also be further converted to ferric hydroxide and then hydrated ferric oxide as seen in Equations 3 and 4. A crevice is created through this destructive process as shown in Figure 1 [11].

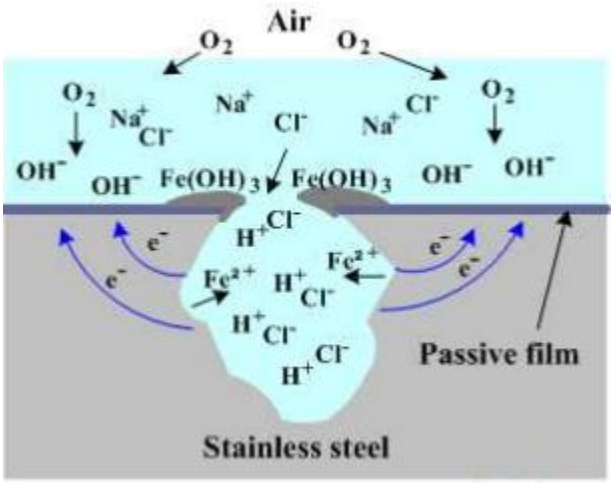

Figure 1: Pitting Corrosion on Stainless Steel

Figure 1 depicts an anodic pit depositing ferric hydroxide on the cathodic surface of the pit.

Additive manufacturing of steel is largely performed in two ways: laser powder bed fusion and direct energy deposition [12]. The focus of this discussion pertains to the latter method: DED. DED is a process where the material being printed is fed either as a

powder or a wire onto the printing surface before being melted by an energy source such as a laser, plasma, or electrical arc. The powder or wire is deposited directly into what is called the melt-pool. In order to further improve the mechanical properties of the deposited material, the wire is heated as it is being fed. Figure 2 depicts what the printer-head looks like for a hot-wire DED [13].

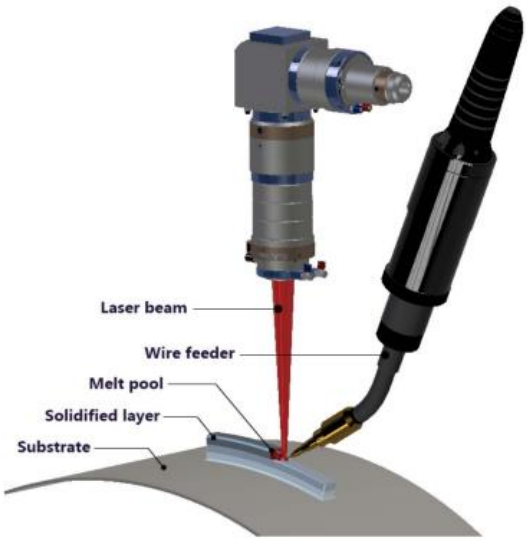

Figure 2: Hot-Wire DED Schematic [13]

Figure 2 depicts a heated-wire depositing directly into a melt-pool of the previously deposited material. A laser is being used to heat the solidified layer. This is similar to what is being used in the Mazak printer that manufactured the tensile samples for this experiment.

The most important part of building reliable parts using a setup shown in Figure 2 are the operating parameters. This includes parameters such as wire feed rate, additive feed rate, laser power, hot-wire power, shielding gas flow-rate, and bead-stepover. By optimizing these parameters, the printed parts are less likely to include defects such as voids, inclusions, and lack of fusion. As most of these parameters are very similar to metal inert gas (MIG) welding, it can be useful to consult a list of process defects that can form if the analogous parameters are set incorrectly. Wire feed rate needs to be appropriate for the speed the part is being printed at, as well as the laser power being used. If the feed rate is too low, the melt pool can be thin and inconsistent in thickness. If the feed rate is too high, the bead width can be excessive and non-

uniform. If laser power is too high, excessive heat can cause the melt to spatter or burn-through, as well as excessively widen the bead width: this can result in distortion of taller parts as the wider than intended beads overlap each other further causing unexpected build-up. Low laser power can result in the layer being convex and not properly melting into the layer below. Improper hot-wire temperature can result in porosity as well as lower than optimal deposition rates [13]. Shielding gas flowrate being too low can result in additional porosity, as well as pin-holes in the layer due to oxidation, as the shielding gas removes oxygen from the environment to reduce or prevent oxide-formation. Excessive gas flowrate can result in poor melt stability and spattering [14]. The wire-diameter will play a role in determining the resolution that a part can be printed at, but must also be balanced with how long it will take the part to be finished. Bead-stepover, or how far the next bead placement from the prior deposition occurred, can play a large role in avoiding porosity, the overall layer height, and the final density of the printed part [15].

The particular machine used in this experiment to produce the SS316L samples was the Mazak VC-500/5X AM HWD. It uses DED with a hot-wire head and has 5-axis of motion; it also comes equipped with a CAT-40, 12,000-rpm spindle for CNC subtractive processing [16]. An image of the Mazak printer used to create the samples used in this experiment can be seen in Figure 135 of the appendix.

Because corrosion is so detrimental to metals used in environments, understanding how corrosion occurs on printed metal parts is important. The goal of this research work is to determine how the four tested print-directions' mechanical properties change after a long-term exposure to a corrosive environment. The two primary metrics of comparison used in this study are mass-loss and tensile-elongation destructive analysis.

Prior research performed by Brand, Moeini, and Marginean has been done regarding direct-energy-deposition with SS316L with corrosion, however it was not a longitudinal study. The study focused on the stickout distance, or the distance from the outlet of the print-head that the wire travels before reaching the melt-pool, and its influence on lack of fusion defects. They quantified their results by analyzing the Brinell hardness of samples produced using varying stickout distances. The hardness testing was a measure of the printed-layer's adhesion strength to the substrate below. Corrosion-resistance of the samples were analyzed using the Tafel test, or potentiodynamic polarization analysis. This method allows for the estimation of the corrosion rate by creating an electrochemical cell with a reference electrode, counter electrode, and the specimen, which creates an electric current across the electrodes through the electrolyte, and then reading the resulting voltage using a potentiostat. The data from Tafel extrapolation allows for a corrosion rate to be determined. Brand, Moeini, and Marginean found that as stickout distance decreased, the corrosion rate, and quantity of lack of fusion defects also decreased. It was also determined that the hardness near regions of lack of fusion measured lower microhardness than areas that did not contain such defects [6].

The research in this study is novel due to the focus on tensile-elongation, printing-direction, as well long-term corrosion that has not been studied simultaneously. It serves to provide more data regarding DED SS316L with a focus on immersion corrosion.

Chapter 2: Materials and Methods

2.1 In-Depth Discussion

Four different sets of print parameters were used to create the various samples. The parameters for each set of samples are listed in Table 2.

Table 2: Print Parameters for each sample from the Mazak VC-500/5x AM HWD

Sample	Build Orientation	Additive Feed Rate (mm/min)	Laser Power (W)	Shielding Gas (L/min)	Wire Feed Rate (in/min)	Hot Wire Power (W)	Bead Stepover (mm)	Layer Height (mm)	Quantity of Samples
A	*Unidirectional 90°*	792	3510	10	165	480	2.5	2.1	11
B	*Unidirectional 0°*	*790*	3510	*20*	165	*450*	2.5	*2.6*	6
C	*Bidirectional 0-45°*	792	3510	10	165	480	2.5	2.1	5
D	*Bidirectional 0-90°*	792	*3545*	10	*166*	*484*	2.5	2.1	10

It can be seen from Table 2 that apart from some minor differences in the magnitude of parameters across sample group's A-D, the primary attribute that sets each sample apart is the build-orientation. The differences from each sample group from Table 2 have been italicized and highlighted for emphasis. The samples used were designed as per the specifications of ASTM E8M subsize (i.e. 6mm gauge width). For reference, the general dimensions of the tensile samples can be seen in Table 3 below along with an annotated diagram in Figure 3 [17].

A detailed description of each build orientation as listed in Table 2 is provided after Figures 4 and 5 and illustrated in Figure 6.

Table 3: Dimensions of the Tensile Elongation Samples in mm

Gauge Length "G"	Width "W"	Thickness "T"	Radius of Fillet, min "R"	Overall Length, min "L"	Length of thin Section "A"	Length of grip section, min "B"	Width of grip section "C"
25	6	1.6	6	100	32	30	10

There are small differences from sample to sample, but the parameters listed in Table 3 are close to the average value for the sample population. For example, some of the samples were

found to be slightly under 1.6 mm in thickness, this is due to the cutting parameters used by the electrical discharge machining (EDM) wire-cutter.

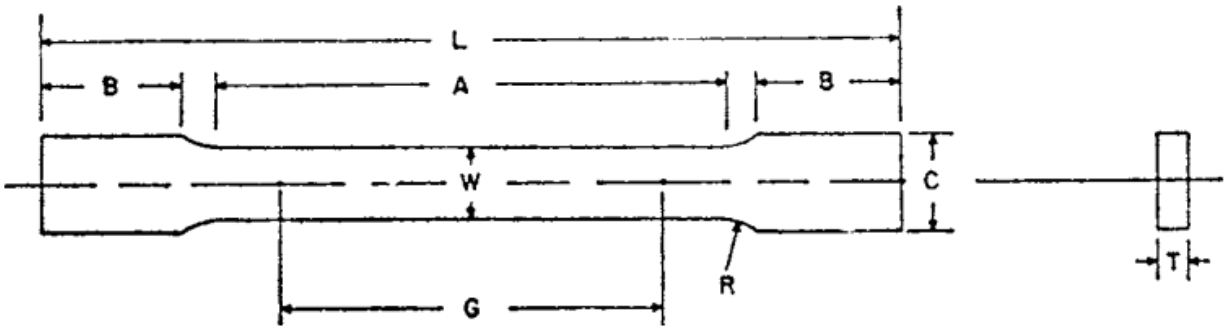

Figure 3: Diagram of Tensile Sample ASTM E8M

The diagram depicted in Figure 3 was pulled from a document listing the standard test methods for tensile-elongation as per ASTM. Note that the diagram is for reference to the annotated dimensions, the tensile-elongation samples in this research were more shaped as seen in Figure 10.

The quantity of samples available for this testing was limited due to other testing that the samples were originally manufactured for. This inconsistent and small sample size is a potential source of error.

All samples were extracted from cuboids printed in the Z-direction such that each layer was coplanar to the “C” and “T” dimensions referenced from Figure 3. That is, the cuboids were printed standing up-right as shown in Figure 4, which shows a comparison of the build of the unidirectional vs bidirectional build-orientations. Figure 5 further explains the build-direction which can be thought of as being inside of the cuboids shown in Figure 4.

Figure 4: a) Unidirectional vs b) Bidirectional Build-Orientations Before Wire EDM

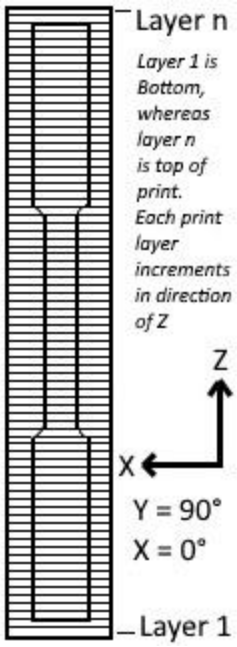

Figure 5: Tensile sample Orientation within the Print-Build

Unidirectional indicates that each layer is printed such that the print-head in reference to the stage are only depositing material moving in one direction, that is, point "A" to point "B" for every row, never point "B" to point "A". Bidirectional indicates that the direction of material deposition alternates with each bead step-over, that is point "A" to "B" for one row, and point "B" to "A" for the following row. Within the same layer, the relative movement of print-head to stage does not change until the layer is complete. This alternating print-direction in each layer can be seen by comparing Figure 4A's unidirectional 0° sample versus bidirectional 0-90°.

In Figure 5, the dark line around the entire figure is the outline of the cuboid as seen in Figure 4, but from a side perspective. When looking at the horizontal lines, each line represents a layer, which lines up with the individual lines seen in Figures 4 and Figure 4A. The outline of the tensile-elongation sample demonstrates where the EDM wire-cutter will remove the test-specimen from the cuboid to achieve the correct final dimensions.

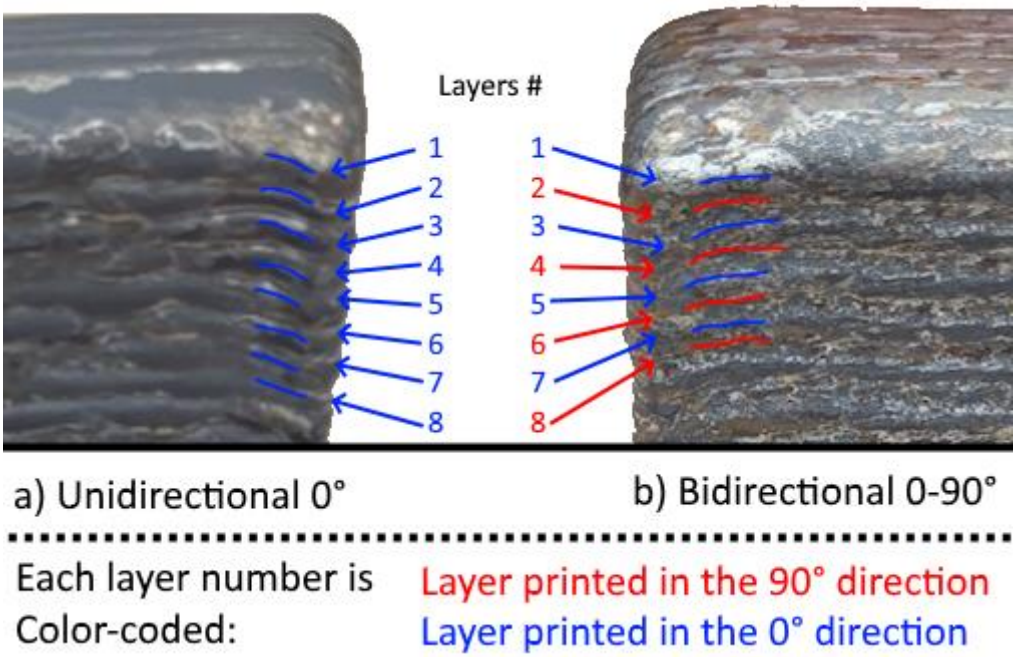

Figure 4A: Magnified Comparison of Unidirectional 0° Versus Bidirectional 0-90° Depicting the Print Directions per Layer

In Figure 4A, each of the printed layers are visible. Blue colors represent layers that were printed in the 0° direction, or right-to-left, whereas the red colors represent layers that were printed in the 90° direction, or front-to-back printing direction. One can see that the printing direction does not change for a) Unidirectional 0°, but the b) Bidirectional 0-90° has an alternating layer pattern. Lines are added after the arrows to help view the contour of each layer.

A layer that is printed in the 90° direction will be normal to the X-Z plane, Y-direction; whereas a print direction of 0° is normal to the Y-Z plane, X-direction, as referenced in Figure 5. Regardless of print direction each layer from all samples were printed coplanar to the X-Y plane, building the sample in the Z-direction. See Figure 6 for a depiction of what each groups build-orientation looks like when viewed parallel to the Z-axis with 0° parallel to left and right.

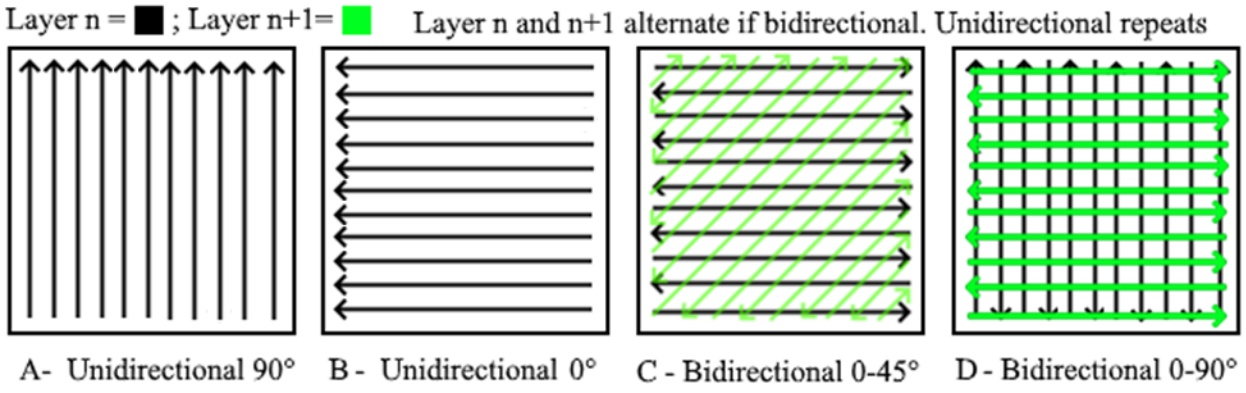

Figure 6: Build-Orientation by Sample Group Represented by Arrows Showing Print Direction

Notice from Figure 6 that unidirectional also only prints in one-direction; that is, if going from a point "A" to "B", after "B" is reached, the printing will stop, and the print-head will restart back on the next line near point "A." Bidirectional will continue at point "B" and go to point "A" on the next line, with the print never stopping.

All samples were extracted from printed-blocks similar to Figure 4 using EDM wire-cutting. Each of the samples shown in Table 3 were machined to the dimensions listed but started as 3D-printed cuboids shown Figure 4.

Corrosion in this experiment is monitored by mass loss, surface profilometry, and microscopy. Surface profilometry is simply a means of analyzing the topography, or 3-D analysis of the surface for features like roughness, crevices, peaks, and other indicators of corrosion. The profilometer used in this experiment is the Keyence VR-5000: One-Shot 3D. When analyzing images, the Keyence VR-5000 uses a rapid array of lights from different angles to scan the surface of interest. If the surface is larger than the area covered by one scan, then the unit will automatically move the stage and scan again until the entire surface has been captured. Once fully scanned, the unit will stitch together all of the individual captures without user intervention and then plot the scanned object as a 3-D surface. The profilometer was utilized routinely

throughout the testing in order to monitor any growing pits and surface alterations that occurred throughout the experiment as well as to capture an optical photo.

For any mass measurements, a Denver Instruments SI-234 scale was used. It has a resolution up to 0.0001 g. In order to reduce potential measuring errors, all mass measurements were repeated three times and averaged. If an obvious outlier measurement was taken for mass, the sample would be removed from the scale and then replaced for a re-measurement. This additional precaution was taken since the mass loss from corrosion was expected to be subtle and meticulous care was needed for reliable mass data.

Prior to beginning the corrosion, all tensile samples were labeled by inscribing a code onto each tensile sample on one side using an electric engraver. This code contained the sample code letter (i.e. A, B, C, or D) and a unique identifying number for each sample (e.g. 1, 2, 5, 11 etc.) based on the location within the build as the samples were cut. Many of these samples already had an existing number written on them with marker; if so, that same number was engraved. The side with the engraved code was declared as the front side of the sample, and the half of the sample the label appears on was declared the top-side of the sample.

In order to preserve the label on the sample as well as prevent corrosion from targeting the grip region labeled “B” in Figure 3 where the engraving occurred, beeswax was utilized as a corrosion resistant film. Beeswax was added to both the top and bottom grip-regions of all samples, including those listed as controls, such that it covered the entire regions labeled as “B” from Figure 3. The Beeswax was purposely terminated in between the regions of “B” and “A” so that the gauge length of the sample was the only portion exposed to corrosion. This method could lead to error in the weight-loss data since the beeswax being applied was hand-dipped and stopped somewhere in the aforementioned region where the sample transitions from the thick to

thinner portion. Differences in exposed surface area from one coating to the next could allow for more or less weight-loss that is unaccounted for in the comparison of one sample to the next. See Figure 7 below for how the beeswax and label were applied to the samples.

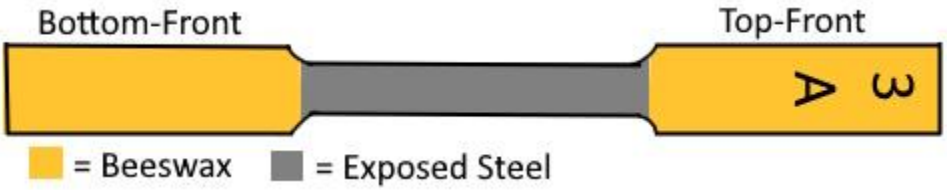

Figure 7: Example Tensile Sample with Label and Beeswax-Coverage prior to Corrosion

If one desired to determine the maximum error that this variability in beeswax coverage can introduce, it is possible to calculate it by comparing the worst-case scenario: a sample with beeswax covering up to measurement "A" from Figure 3 versus beeswax only covering up to measurement "B." This is the worst-case since you would be comparing the minimum area exposure to the corrosion environment versus the largest area of exposure. It turns out that this can introduce up to an absolute maximum of 30.6% error for one given reading in the corrosion weight loss data. The smallest exposed area on one side of the tensile sample is 192 mm^2; the largest exposed area on one side of the tensile sample would be 250.808 mm^2. By coating the beeswax by hand, the top-facing area (excluding the sides) has a possible value of 221.404±29.404 mm^2. See Figure 8 for the region that is 29.404 mm^2.

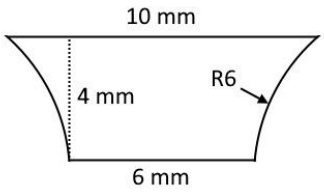

Figure 8: The Transition Region from the Thin to the Thick Portion of the Tensile Sample

The full method of calculating the area is outside the scope of this discussion, but it can be summarized by first calculating the area of the green-shaded region of Figure 9 using

geometry and integration, multiplying this value by two, and then adding it to the 6x4 mm rectangular region inside the shape shown in Figure 7.

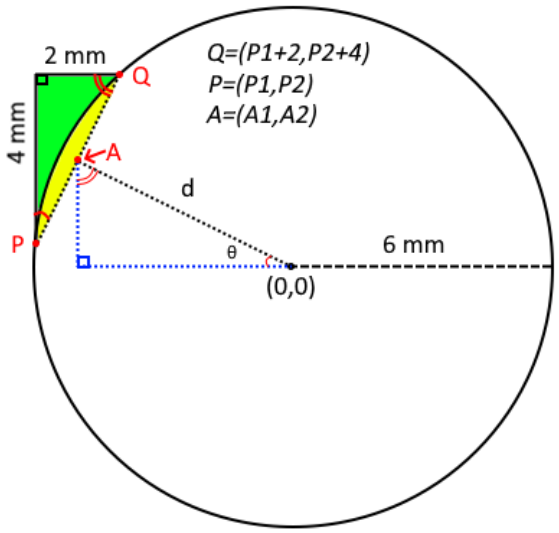

Figure 9: Diagram for Calculating Part of the Area of Figure 8

Using the formula for a chord of a circle allows for the determination of "d." "A" is perfectly between "P" and "Q."

The actual corrosion was performed using 1.0 M HCl prepared from reagent grade fuming hydrochloric acid, i.e. 37% w/w or 12.178 M HCl. The beeswax-coated samples were immersed into two separate glass Pyrex baking dishes with the front-side of the samples facing upwards for each immersion. The samples were spread apart such that no two samples were touching. The room temperature conditions of the corrosion were not monitored during the course of the experiment, but it was likely within 74±5°F throughout the test duration; however, this should not matter, as all samples would have been exposed to the same conditions so that their weight-loss relative to each other would still be reliable. The samples received no form of solution agitation in the baking dishes during immersion. There was also a thin piece of polyethylene food-wrapping paper lightly placed over the top of the dishes; this was done to prevent the evaporation of water, which would change the molarity of the HCl, as well as preventing debris from falling into the dishes.

Upon removing samples from the dishes containing 1.0 M hydrochloric acid, samples were immediately rinsed with deionized (DI) water and dried off using paper towels. Before weighing or doing profilometry, the beeswax was removed entirely. The method to remove the

beeswax was meticulous but necessary to ensure that residual beeswax was not present to erroneously increase the post-weight from corrosion. First a plastic scoop was utilized to mechanically remove the bulk of the beeswax back into a melting pot. Plastic was used intentionally as to not scratch the surface of the samples which would promote localized corrosion. Next a glass dish was heated on a hot-plate to around 155°F; this is above the melting point of beeswax, which is around 145°F. The samples were placed on the hot plate, rotated a few times, and wiped off with a paper towel. In order to completely remove any residual beeswax, each sample was immersed in heated n-heptane using a small glass petri dish. The heptane was heated carefully in a fume-hood with no sources of ignition nearby. The heated heptane dish was constantly monitored for safety concerns. Once any residual beeswax was dissolved, the samples were once again dried with a paper towel and were then ready for measurements and profilometry.

At the conclusion of the corrosion testing, all tensile samples were broken using tensile-elongation testing units, specifically Instron. Two separate machines were used simultaneously for each sample: Instron 5967 for load-force data and Instron 5500R for strain data. The reason for this is that the load data from the Instron 5500R unit was not reliable as the clamps would occasionally slip off the sample; however, it has a port for an extensometer to be utilized. The Instron 5967 did have reliable load-force data, but the existing extensometer was incompatible with the 5967 unit. In order to properly pair the data from the two separate units, the samples were loaded onto the load-cells of the Instron 5967 and the extensometer which was plugged into the Instron 5500R was properly affixed to the sample. At the start of each pull-test, both units were calibrated and zeroed out. When ready, both units were started simultaneously such that the

recorded values for time = 0 seconds would be almost identical on both units. This allows one to splice together force and strain data together without needing to trim the data or synchronize it.

Once the samples were broken, the fracture locations on both the top and bottom of each dog-bone were analyzed on a Keyence VHX Digital microscope. Glare-removal was enabled and all pictures were taken at 100x magnification. These images were taken to document any defects located within the fracture-zone as well as monitor the internal progression of corrosion.

The 32 samples were split into groups of controls, which received no corrosion but had all other processing steps; 21-day corrosion samples which received approximately 504 hours of corrosion before being tensile tested; and 43.5-day corrosion samples which received approximately 10041.2 hours of corrosion prior to being tensile tested. Table 4 below lists all 32 samples according to which type of sample they were.

Table 4: The Corrosion Duration for each Sample

Sample Code	HCl Immersion Duration	Sample Code	HCl Immersion Duration
TA	Control	10B	Control
1A	21 Days	3C	21 Days
2A	43.5 Days	4C	43.5 Days
3A	Control	5C	21 Days
4A	21 Days	8C	43.5 Days
5A	43.5 Days	11C	Control
6A	Control	1D	Control
7A	Control	2D	21 Days
8A	43.5 Days	3D	43.5 Days
9A	21 Days	4D	Control
BA	Control	5D	21 Days
3B	21 Days	6D	43.5 Days
4B	43.5 Days	7D	Control
5B	Control	8D	43.5 Days
8B	21 Days	9D	21 Days
9B	43.5 Days	10D	Control

Table 5 shows the groupings of each build of samples, with the appropriate letter abbreviation, with the number of samples for the control, 21-days, and 43.5-days exposure.

Table 5: Summary of Table 4 by Quantity of Samples per Category

Sample Code	Controls	21-Days	43.5-Days	Total
A	5	3	3	11
B	2	2	2	6
C	1	2	2	5
D	4	3	3	10
Total	12	10	10	32

One may notice a disproportionate amount of control samples in each group. This was caused by two separate issues. The first issue resulted from the use of remaining samples – some builds had more samples than other builds, so where more than six samples were available, the remaining number became controls. In addition, some samples had a drastically different appearance on the surface compared to the rest of the samples. All samples that were set to be corroded for either 21 days or 43.5 days had a similar appearance at the beginning of the experiment. By not mixing the different appearance samples into corrosion testing, results that were affected by surface differences would not create a bias in results. This was done to ensure that every group had at least two samples per corrosion category that would be less likely to differ significantly during corrosion. Figure 10 shows a comparison of a typical looking sample compared to one that was designated as a control sample by appearance only.

Figure 10: Comparison of Dull Sample Versus Shiny

Most of the samples prior to any corrosion had the dull appearance as seen in the top image of Figure 10, which is the result of the EDM wire-cutter. The samples that had the shiny appearance had a dull appearance when flipped over. This is because the samples started as cuboids shown in Figure 4 were then machined into the shape of the ASTM E8M, and then sliced into thin 1.6 mm thick samples. The shiny samples were on the very ends of the machined, unsliced block as shown in Figure 11.

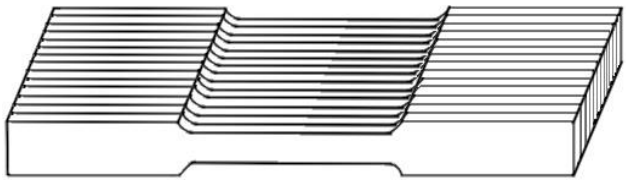

Figure 11: Sample Block Prior to Plasma EDM

Figure 11 depicts the tensile samples immediately after being machined but before being sliced by plasma EDM. Lines were added to depict how the individual tensile samples appeared after the EDM wire-cutting process was finished.

All of the individual details have been discussed about each facet of the experimental process, although the overall process has not been laid out chronologically; the following discussion describes the overall process to conduct this experiment.

2.2 Chronological Process

Initially, the samples were engraved with the appropriate letter representing the build and the number, indicating the location within the build. The samples were weighed on a mass scale and the mass values were recorded in a journal. Afterwards, the samples were scanned on a profilometer to capture the surface topography. The beeswax was applied to each of the samples, by first melting the beeswax and then dipping the samples to protect the regions that are not to be corroded. After the samples are coated, a 1.0 M HCl solution is made up and carefully poured into two Pyrex baking dishes; each dish contained 1 L of solution. The samples designated for 21-days and 43.5-days of corrosion were immersed in the hydrochloric acid filled dishes and then covered with a polyethylene film. No samples were overlapping and all had their front-side facing upwards (etched label upwards). The date and time of the samples' immersion were recorded in a journal. After approximately seven days have elapsed, the samples were removed from the hydrochloric acid solution, rinsed, and dried off. The date and time of removal were recorded in a journal. The beeswax was then removed completely.

This weighing, profiling, and protecting processes as described above were repeated until the 21-days and 43.5-days corrosion durations were met. The control samples were not immersed in the hydrochloric solution but followed the rest of the preparation process, including coating with beeswax and removal of beeswax along with the other samples.

Due to an error, all the control samples received some corrosion but were removed after 16.7 hours. This is a source of error but it is unknown as to the magnitude of the error as all control samples were affected. However, as most damage from corrosion occurs due to long-term exposure, it is expected that this error is minimal.

After the allotted corrosion duration was met, the samples were broken using the tensile elongation units and the stress and strain data were spliced together. The sample fracture locations were analyzed on a digital microscope at 100x magnification and images of both the top and bottom portions of the samples were saved.

Chapter 3: Results

Figure 12, 13, and 14 shown below depict the mass over time for the 43.5-day, 21-day, and control samples.

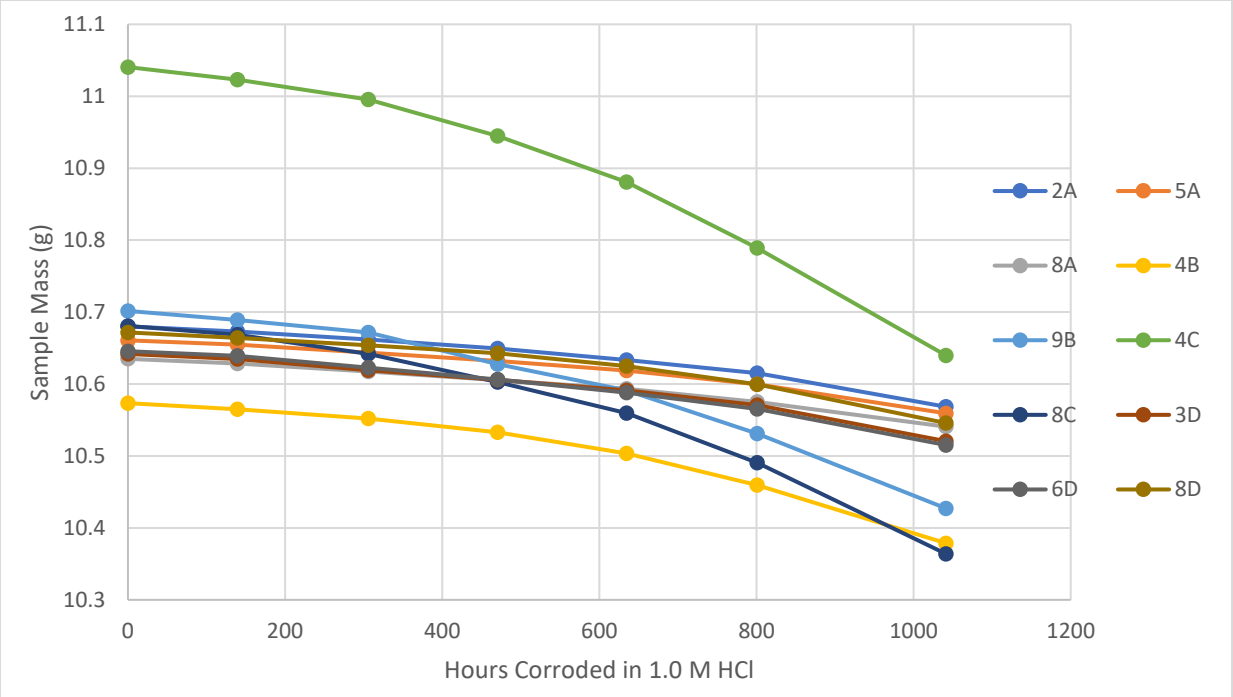

Figure 12: Mass-Loss over Time for 43.5-Day Corrosion Samples in 1.0 M HCl

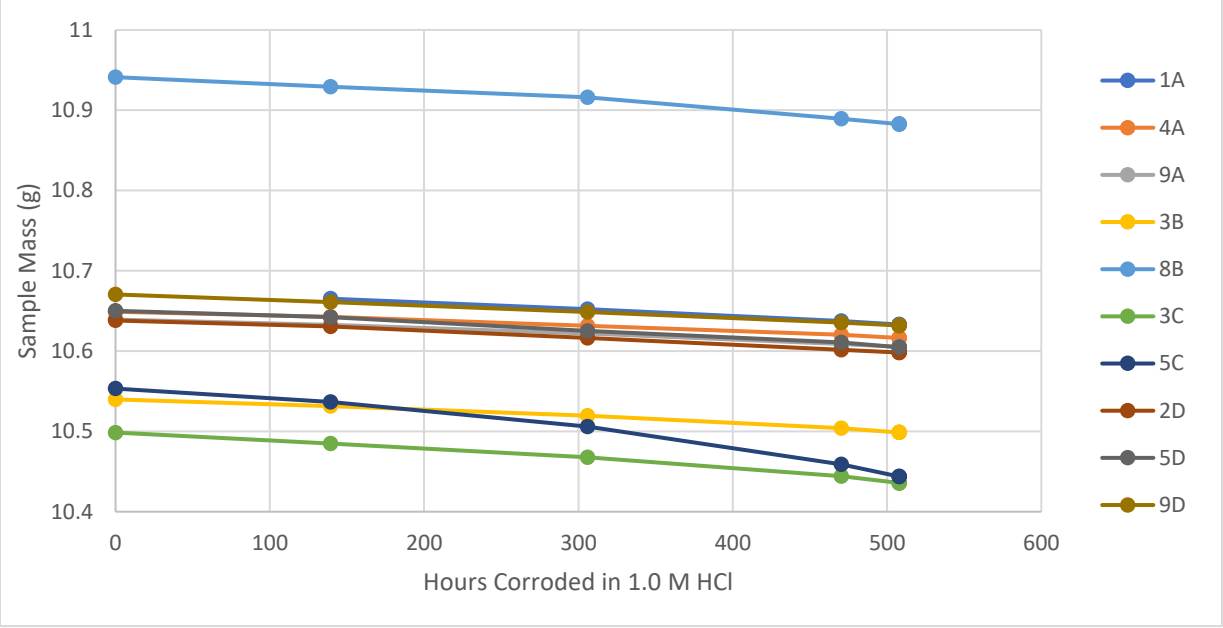

Figure 13: Mass-Loss over Time for 21-Day Corrosion Samples in 1.0 M HCl

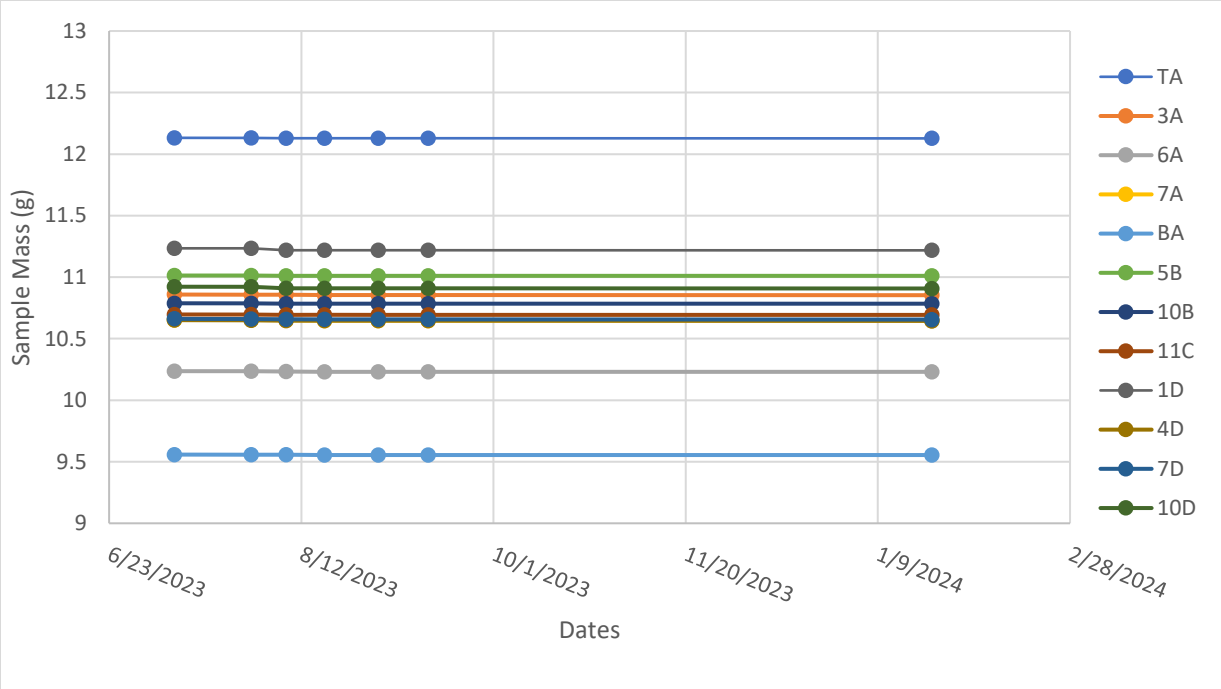

Figure 14: Mass-Loss by Date for Control Samples

When looking at Figure 12, the X-axis covering the time covering the time covers the full 43.5 days, which is 1044 hours. The Y-axis is the sample mass, which varied slightly for each sample. When looking at the data, one can see that all samples lost weight. However, there are no distinct trends because of the differences in starting weights. For figure 13, the X-axis covers the time for 21 days, which is 504 hours. As with Figure 12, the data has a great spread due to the individual weights of the samples, so no distinct trends could be seen. Figure 14 shows the various days that the control samples were weighed, so the X-axis. Looking at each control, there is no discernable weight loss. As with Figures 12 and 13, though, there is a wide range in initial weights.

It is important to keep in mind the differences in scales when comparing Figures 12, 13, and 14. It can be seen that not all the samples started with identical masses, this is due to varying sample thicknesses. To account for this, the weight-loss over time for each sample was

normalized and re-plotted in Figures 15, 16, and 17 for a better comparison. The samples were normalized by dividing the samples' current mass by their initial mass; this results in all samples starting with a normalized mass of 1.0 and decreasing according to how much of the initial mass has depleted due to corrosion.

When looking at Figures 15 and 16, for all builds, one can see that there is a minimal weight change between weeks 0 and 1. Between weeks 1 and 2, again for all builds, there is a gradual drop in weight. After week 2, though, there is a drastic increase in weight loss, with the two C builds losing the most in both Figures 15 and 16, followed by the two B builds, shown most clearly in Figure 15.

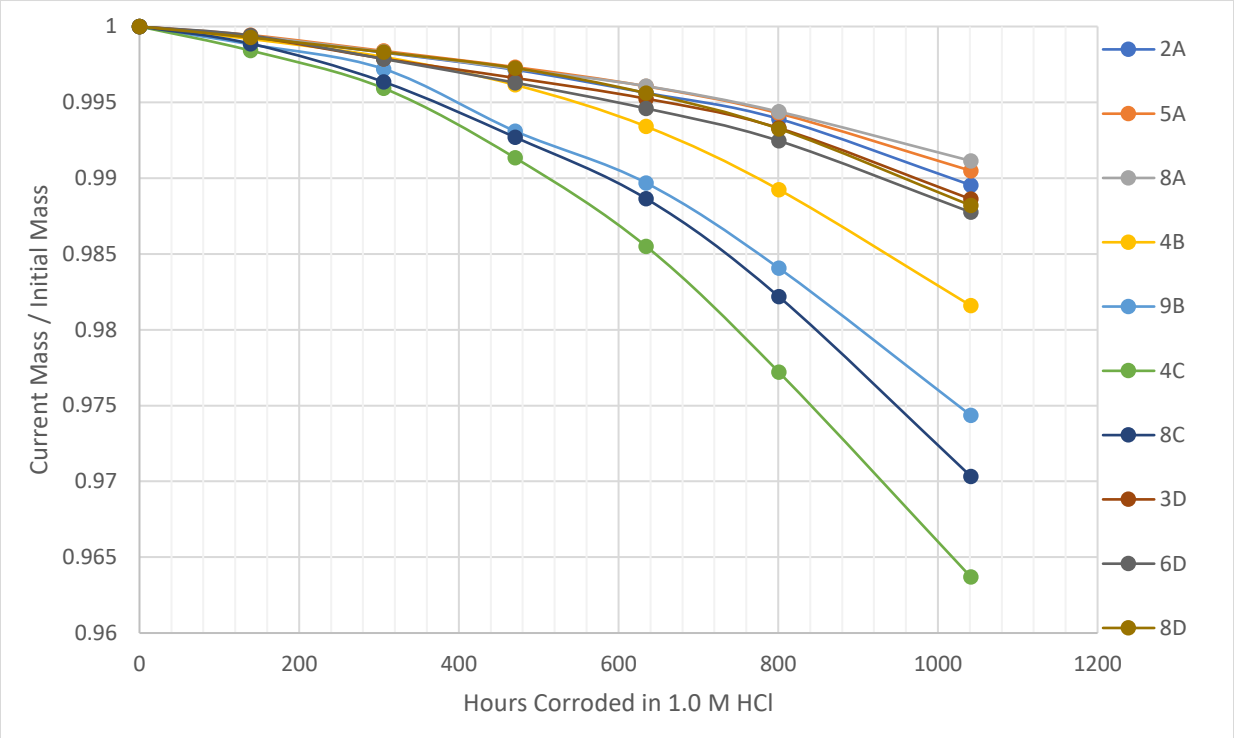

Figure 15: Normalized Mass-Loss over Time for 43.5-Day Corrosion Samples

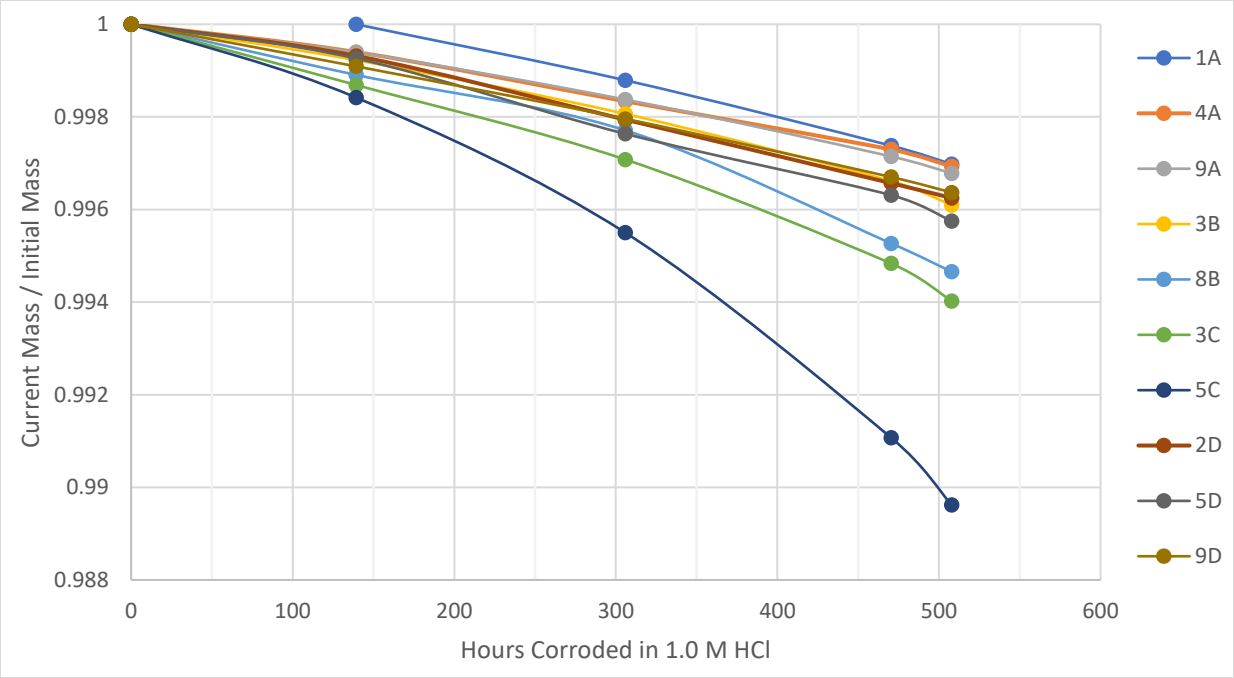

Figure 16: Normalized Mass-Loss over Time for 21-Day Corrosion Samples

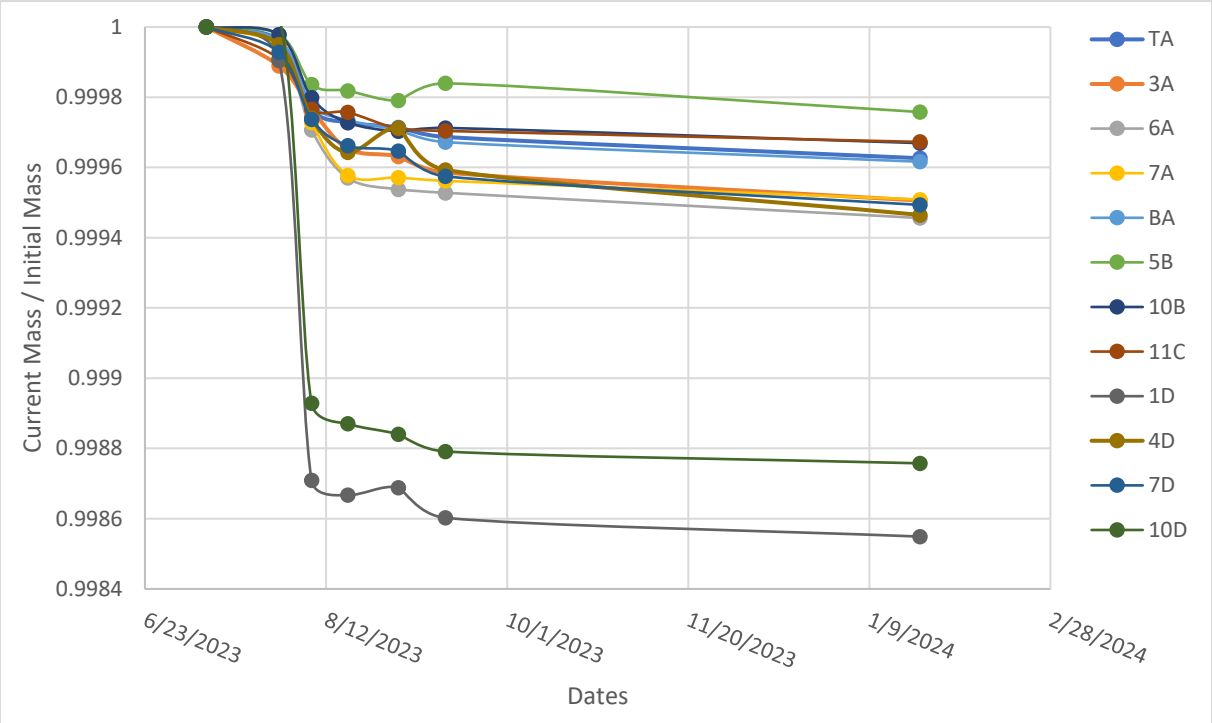

Figure 17: Normalized Mass-Loss by Date for Control Samples

Again, it should be noted the differences in scales for each of the graphs. One can see that the control samples showed an apparent large drop in normalized mass on 8/8/2023. This was due to an accidental exposure of the control samples to the hydrochloric acid immersion baths. The total duration the control samples were in the corrosion bath was 16.67 hours. This exposure is visible only in the control mass-data and is nearly imperceptible from the non-normalized data (Figure 14). It is also, truly, very minimal, resulting in, at most, a decrease of around 0.14% mass, a very small amount. Compare this to the mass-loss of the 21-day and 43.5-day samples which experienced a change of 1.1% and 3.6% total mass, which is magnitudes greater than that of the control group.

In order to better compare each of the sample groups (i.e. A, B, C, and D), the average weight-loss per sample type was plotted on the same chart, as shown in Figure 18, so that it is easier to comprehend the data. Error bars representing ± one standard deviation is displayed on each average mass corresponding to the appropriate corrosion duration.

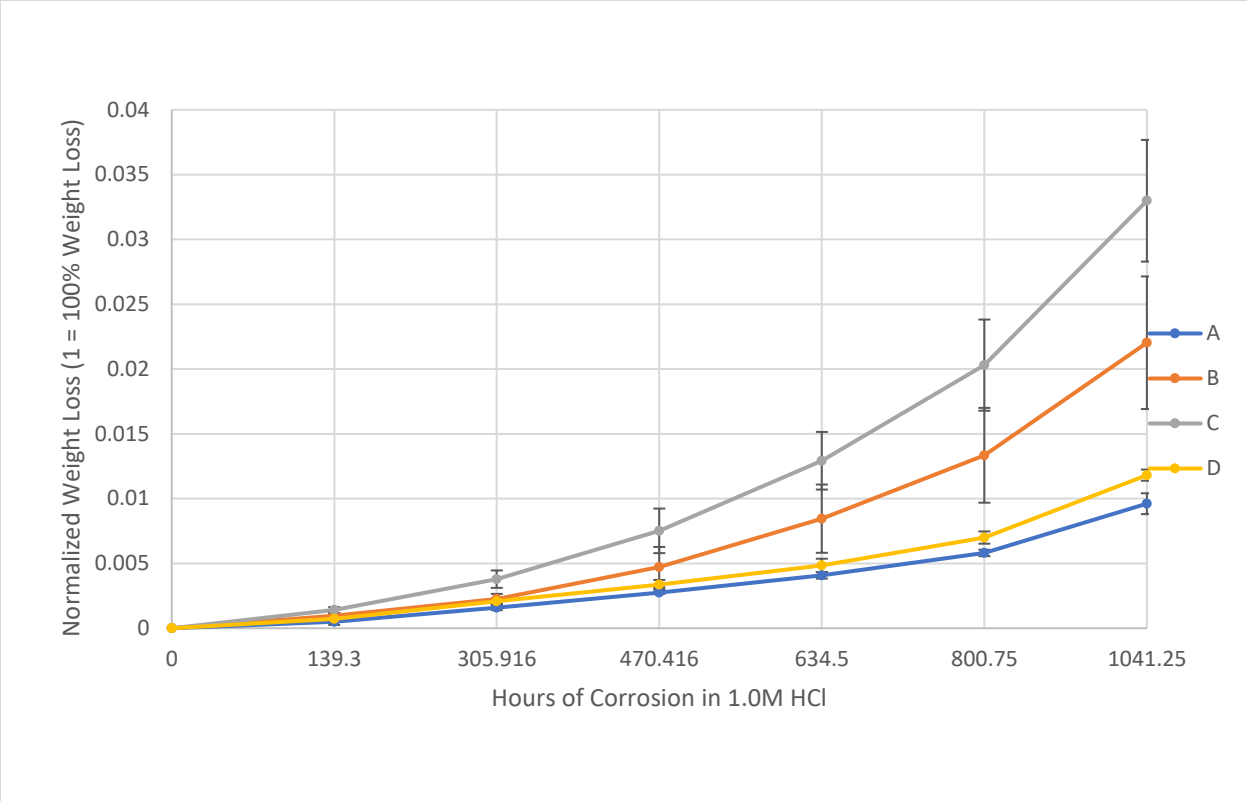

Figure 18: Normalized and Averaged Mass Data by Sample Type with Error Bars Showing ± One Standard Deviation

Note that Figure 18 is formatted such that each sample starts at a value of 0. To convert between the y-axis of Figure 18 and Figures 12 through 17, one simply needs to subtract Figure 18's y-axis values from 1. When looking at Figure 18, there is no big difference between the four builds prior to one week of corrosion. At two weeks of corrosion, build C is beginning to separate from the other builds, but builds A, B, and D still mostly overlap. There is further separation at week three, where builds B and C begin to clearly separate, while builds A and D stay close. At the end of six weeks of corrosion, build C has clearly corroded more than build B, which has also clearly corroded more than builds A and D.

In order to determine whether there is a statistically significant difference between the sample groups, a one-way ANOVA analysis was performed. Analyzing the sample groups at corrosion hour 1041.2 yielded an F-Value of 32.245. The critical value for an alpha level of 0.01 with a numerator degree of freedom of 4 and a denominator degree of freedom of 6 as per this data set is 9.15. Since the calculated F-value is greater than the critical F-value from a standard F-distribution table, one can conclude that at least one of the sample groups has a mean statistically different from the rest at confidence level of 99%.

From Figure 18, one can see that the standard deviation bars and means of sample groups B & C as well as A & D are the closest to each other in terms of approaching overlap. In order to determine if all group's average mass data is statistically different than each other, a two-sample T-Test was performed on both the aforementioned pairs. Visually, it appears that variance is similar between groups B & C as well as A & D, so a non-parametric test is unnecessary. For groups A & D, the T-Test value (two-tailed) is 5.12 and the critical T-value is 4.604 at an alpha level 0.01; therefore, one can say at 99% confidence that groups A & C have statistically different means. For Group B & C, the T-Test value was calculated at 3.15 with a critical T-Value of 2.92 at an alpha level of 0.1; this means that one can say at a 90% confidence level that the means of groups B & C are statistically different. Groups B & C are much closer to each other than A & D, statistically, because of the standard deviation, shown as error bars in Figure 18.

Since the data is being shared in both a cumulative means of showing total corrosion hours as well as the dates the masses were taken, in the case of the control samples, it is beneficial to list the cumulative hours of corrosion achieved by sample type by the date it was reached. Refer to Table 6 below for this summary.

Table 6: Cumulative Corrosion Duration in Hours for 21-Day, 43.5-Day, and Control Samples by Date

Sample Type	7/10/23	7/30/23	8/8/23	8/18/23	9/1/23	9/14/23	1/23/24
21-Day	0	139.3	305.9	470.4	507.8	507.8	507.8
43.5-Day	0	139.3	305.9	470.4	634.5	800.7	1041.2
Control	0	0	0	16.6	16.6	16.6	16.6

In Figures 19, 20, and 21 below, the tensile elongation results are reported for each sample group according to the corrosion duration; this includes the ultimate tensile strength, yield strength taken at 0.2%, and Young's modulus.

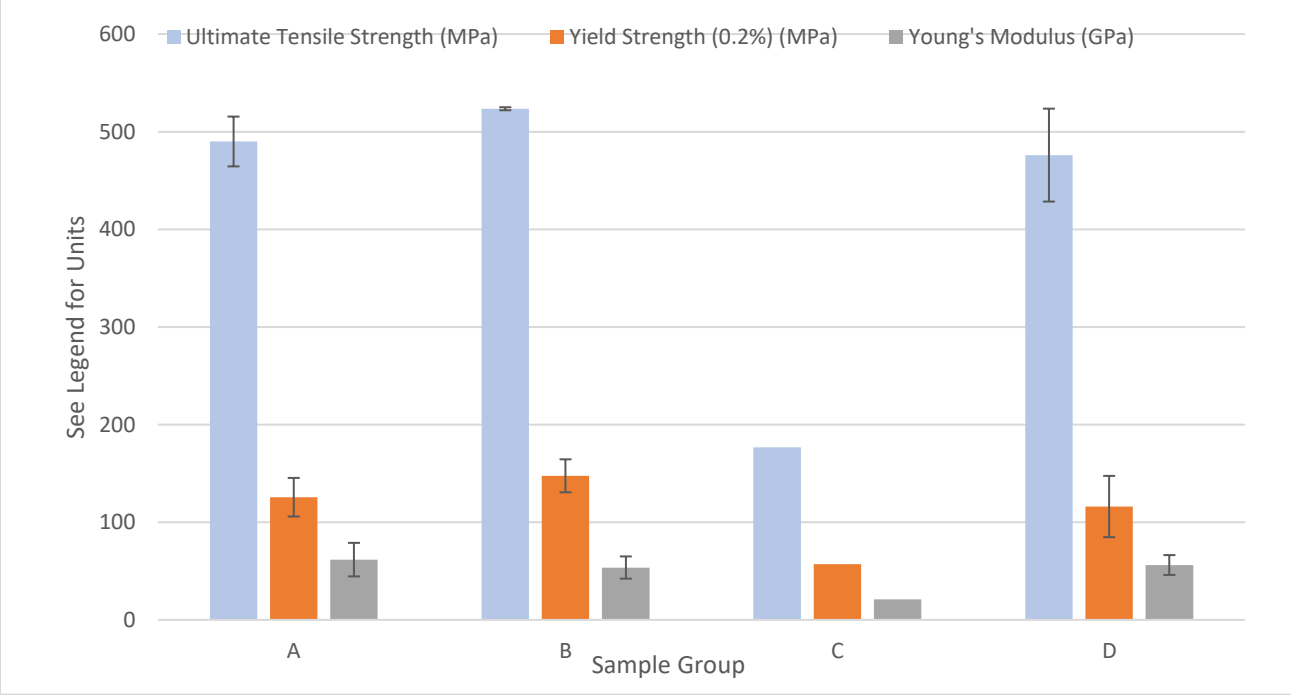

Figure 19: Tensile Elongation Properties of each Sample Group for the Controls with ± One Standard Deviation as the Error Bar

Figure 19 shows that sample group C was an outlier for low mechanical properties. The other builds all had similar ultimate tensile strength, yield strength, and Young's modulus when

comparing the control samples without any corrosion performed.

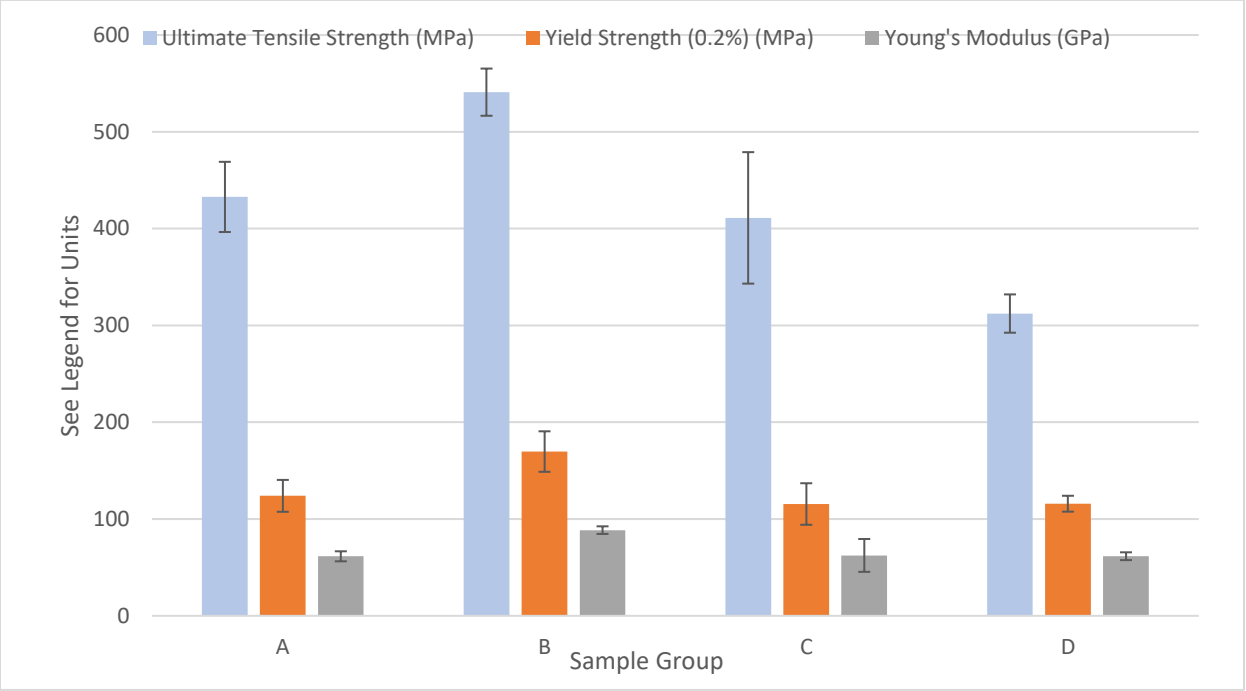

Figure 20: Tensile Elongation Properties of each Sample Group for 21-Day Corrosion with ± One Standard Deviation as the Error Bar

After 21 days of corrosion, builds A and C were surprisingly similar ion ultimate tensile strength, since the control for C was so low. Build B had the highest ultimate tensile strength, while build D dropped significantly in ultimate tensile strength after 21 days. For the yield strength, build B was higher than build A, which was higher than builds C and D. For Young's modulus, build B was higher than builds A, C, and D.

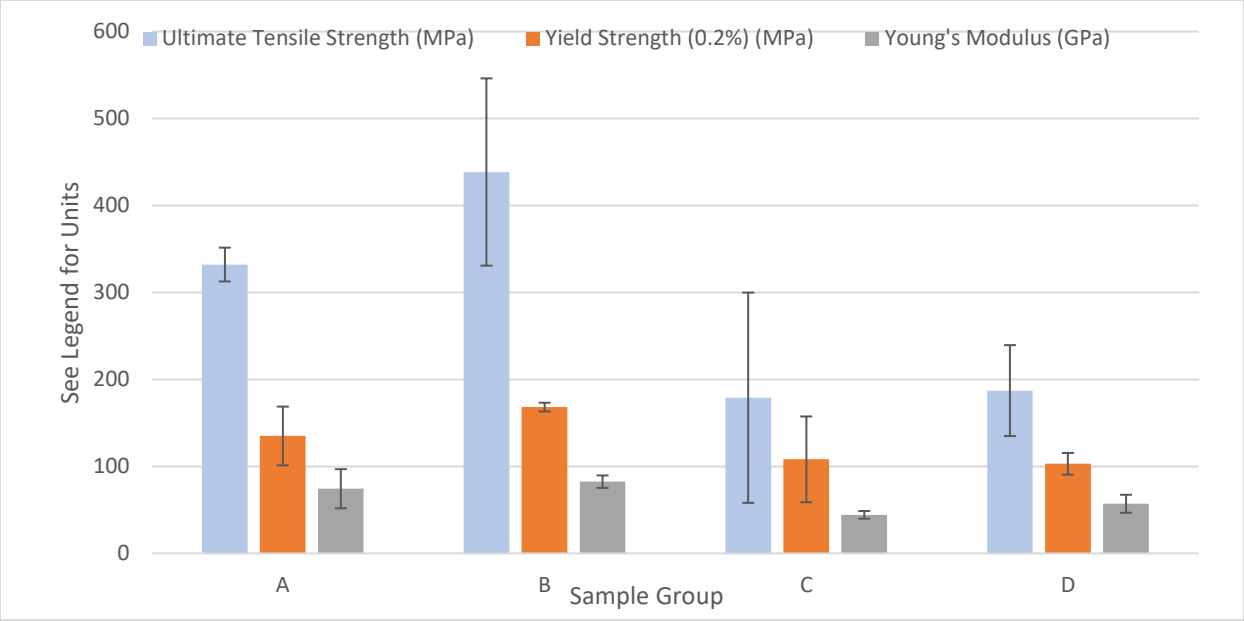

Figure 21: Tensile Elongation Properties of each Sample Group for 43.5-Days Corrosion with ± One Standard Deviation as the Error Bar

After 43.5-days, build B had the highest ultimate tensile strength, followed by build A, then build C and D. For the yield strength, build B was higher than build A, which was higher than builds C and D. For Young's modulus, build B was higher than build A slightly, with both being higher than builds C and D.

Figures 19 through 21 displayed the individual tensile elongation properties as a comparison from group to group, but it can be useful to also view each tensile property independently as a function of corrosion duration. That is, comparing the control samples to 21-day and 43.5-day samples per parameter. Figures 22 through 24 below depict the data as described for ultimate tensile strength, yield strength at 0.2% strain, and Young's modulus.

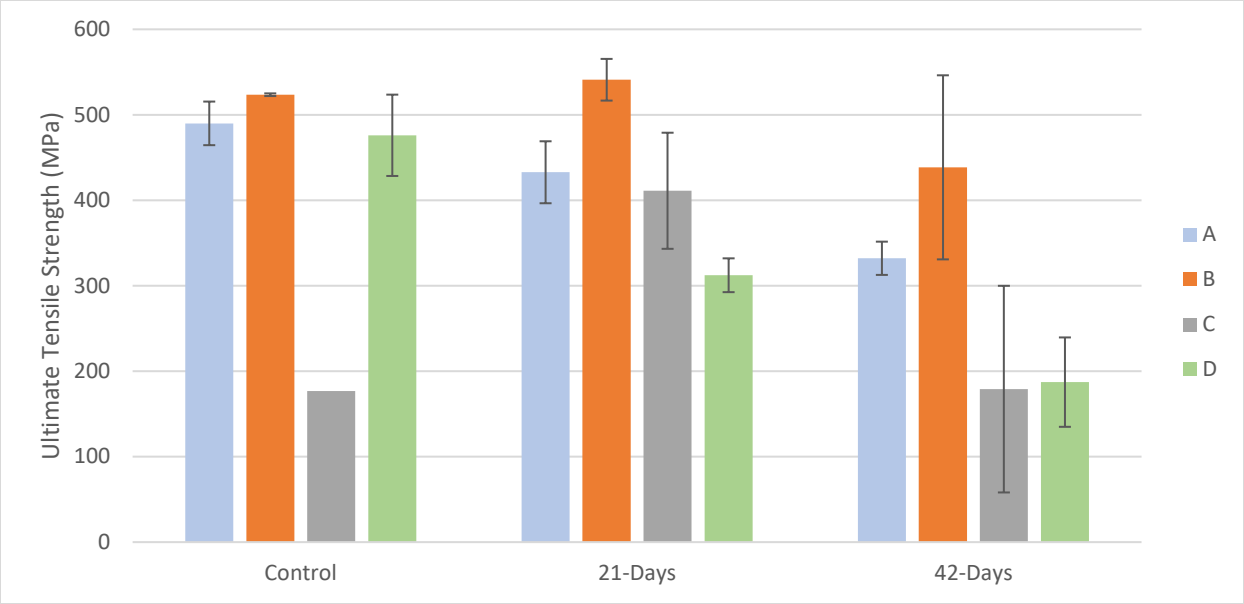

Figure 22: Ultimate Tensile Strength of each Sample Group Comparing the Controls, 21-Days, and 43.5-Days Corrosion Duration with ± One Standard Deviation as the Error Bar

When looking at Figure 22, the ultimate tensile strength decreased from 0 to 21 days and from 21 days to 43.5 days for build A and build D. For build B, there was no real decrease from 0 to 21 days, followed by a decrease from 21 days to 43.5 days. Build C showed an increase in ultimate tensile strength from 0 to 21 days, followed by a decrease from 21 to 43.5 days, where it was roughly the same as 0 days. Part of this behavior is likely due to the few samples of build C available for testing.

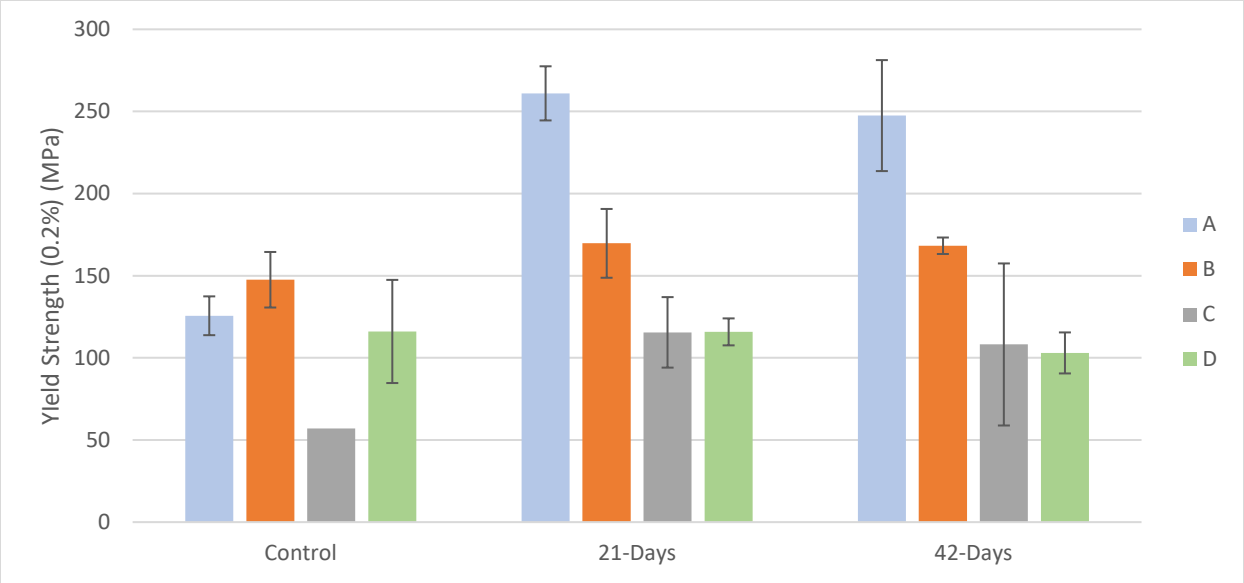

Figure 23: Yield Strength at 0.2% Strain for each Sample Group Comparing the Controls, 21-Days, and 43.5-Days Corrosion Duration with ± One Standard Deviation as the Error Bar

When looking at Figure 23, the yield strength surprisingly increased from 0 to 21 days and remained the same from 21 to 43.5 days for builds A and C. For build B, the yield strength slightly increased from 0 to 21 days and then remained roughly the same from 21 to 43.5 days. For build D, the yield strength roughly remained the same from 0 days to 43.5 days.

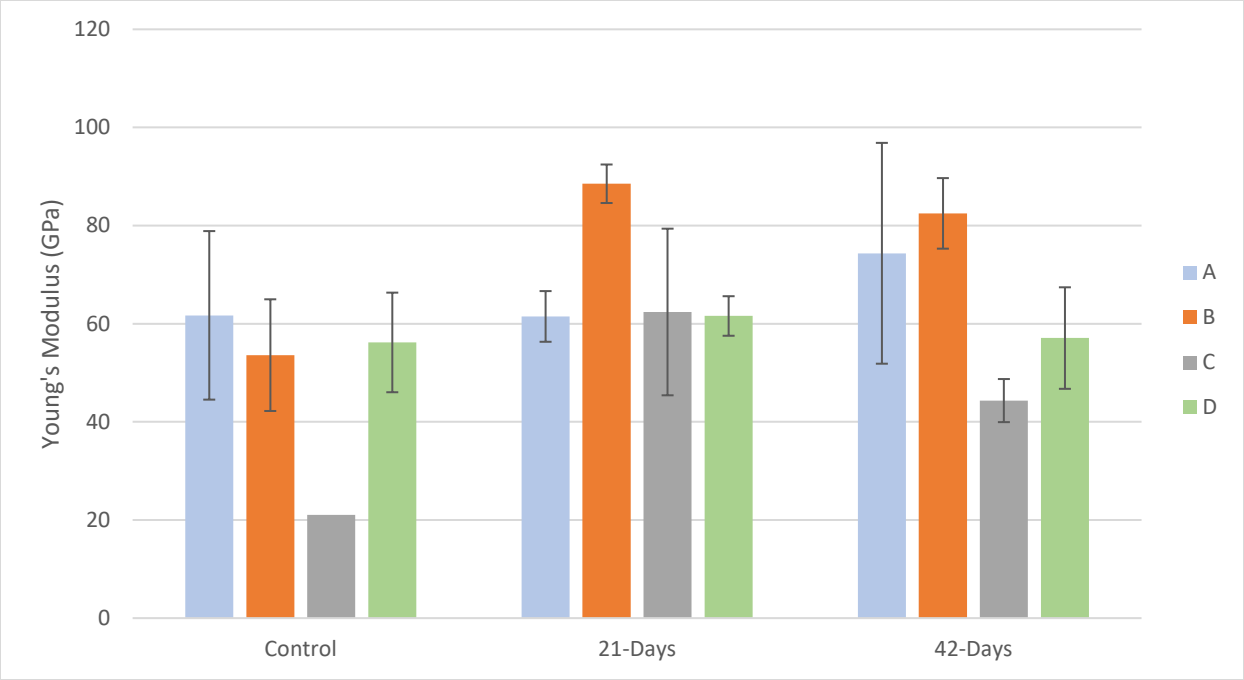

Figure 24: Young's Modulus of each Sample Group Comparing the Controls, 21-Days, and 43.5-Days Corrosion Duration with ± One Standard Deviation as the Error Bar

Figure 24 shows the Young's modulus. All four builds show an increase in Young's modulus from 0 to 21 days. All four builds then show roughly the same Young's modulus after 43.5 days, when the error bars are included within the calculations.

The following Figures 25 through 56 depict the stress over time graphs created from the stress-strain data by the tensile-elongation testing units. It was decided to depict the charts as stress versus time instead of strain due to the extensometer slipping off of many samples as the magnitude of elongation increased. This was inconsequential to the overall data as the strain is needed in the elastic region of the stress-strain curve for calculation of Young's Modulus. It is useful to see the stress as the sample breaks in order to determine whether the fracture was brittle or ductile; the declaration of fracture-type will be listed when describing the fracture-points of each sample following the stress versus time charts.

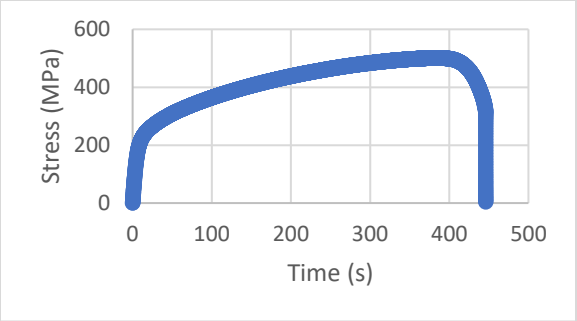

Figure 25: Stress vs Time of Control Sample 3A

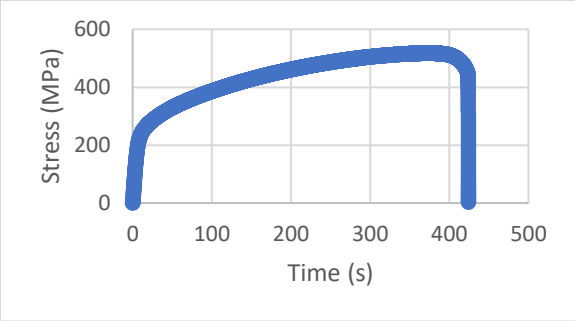

Figure 26: Stress vs Time of Control Sample 6A

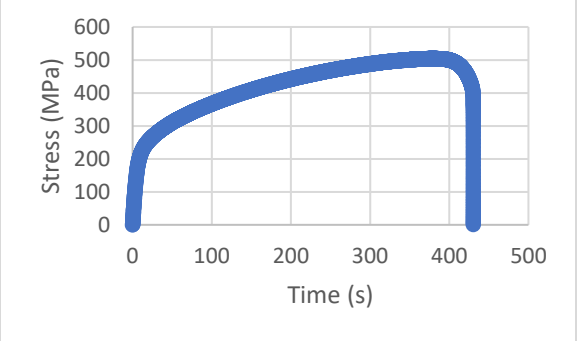

Figure 27: Stress vs Time of Control Sample 7A

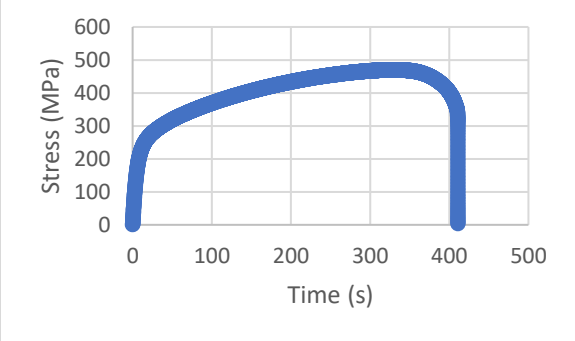

Figure 28: Stress vs Time of Control Sample BA

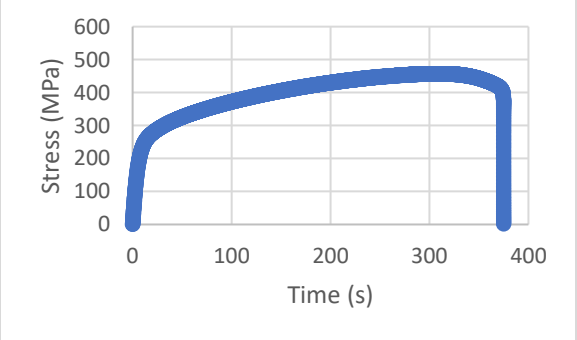

Figure 29: Stress vs Time of Control Sample TA

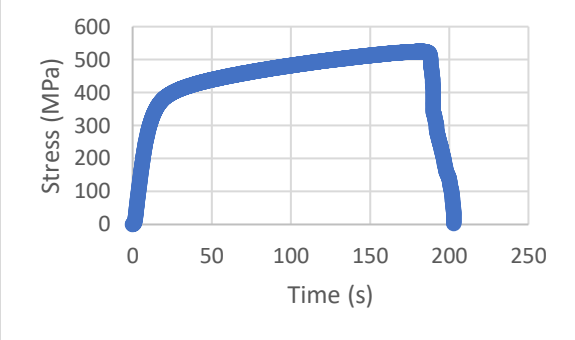

Figure 30: Stress vs Time of Control Sample 5B

The right side of Figure 30 for sample 5B is starting to show some signs of brittle

fracturing since the fracture-point is not a sudden decrease in stress from the current load to 0, but rather a slope. It is still mostly vertical and so the fracture in this test is being considered mostly ductile.

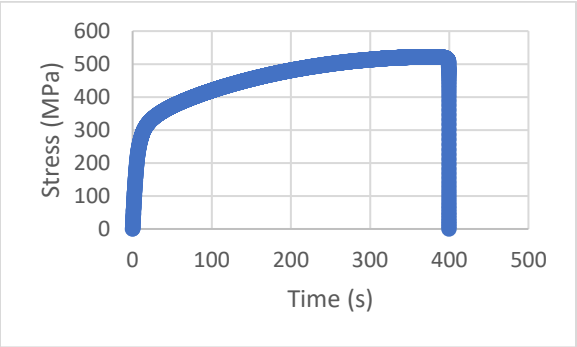

Figure 31: Stress vs Time of Control Sample 10B

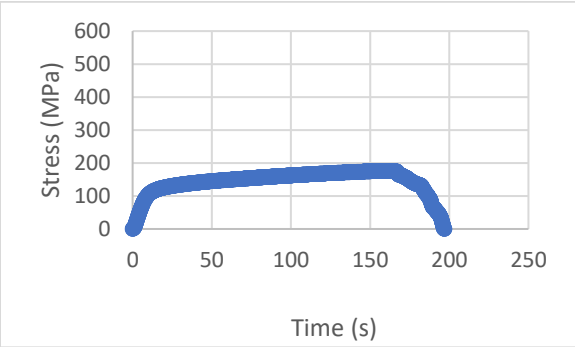

Figure 32: Stress vs Time of Control Sample 11C

11C from Figure 32 is the first full brittle break. The ultimate tensile strength, or the maximum point in the chart is substantially lower than the rest of the control samples as well as having a slope to the fracture point.

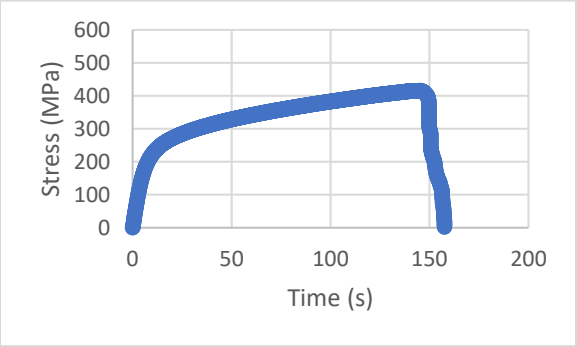

Figure 33: Stress vs Time of Control Sample 1D

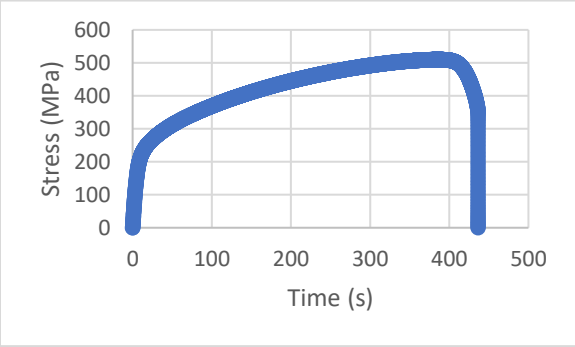

Figure 34: Stress vs Time of Control Sample 4D

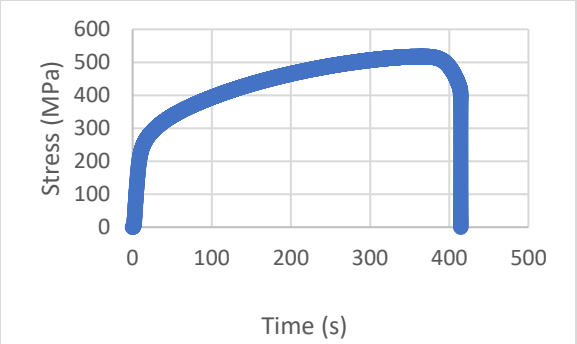

Figure 35: Stress vs Time of Control Sample 7D

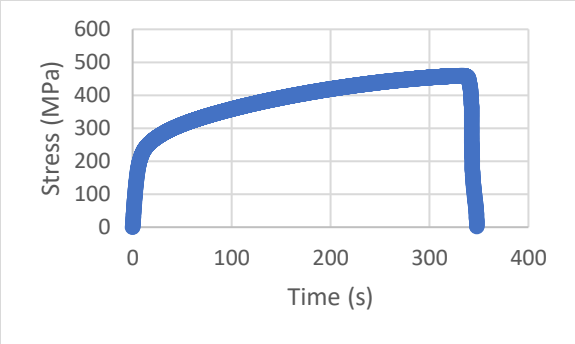

Figure 36: Stress vs Time of Control Sample 10D

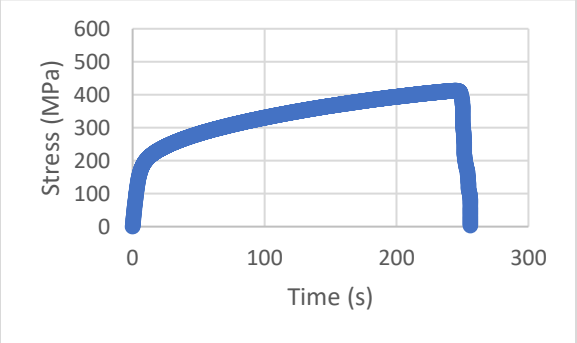

Figure 37: Stress vs Time of 21-Day Sample 1A

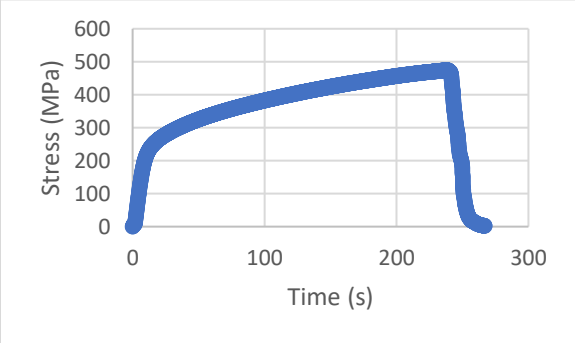

Figure 38: Stress vs Time of 21-Day Sample 4A

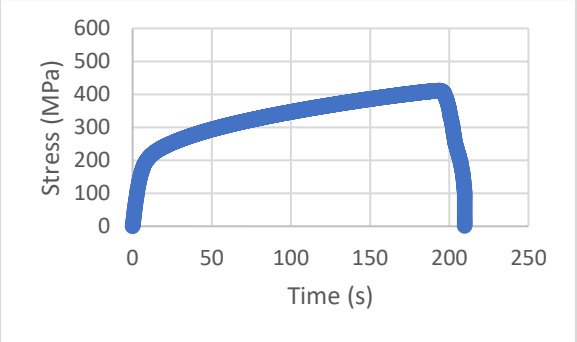

Figure 39: Stress vs Time of 21-Day Sample 9A

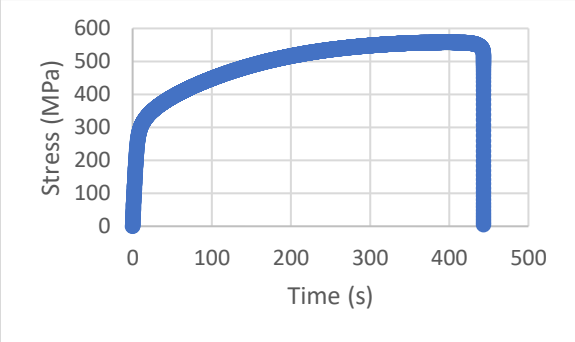

Figure 40: Stress vs Time of 21-Day Sample 3B

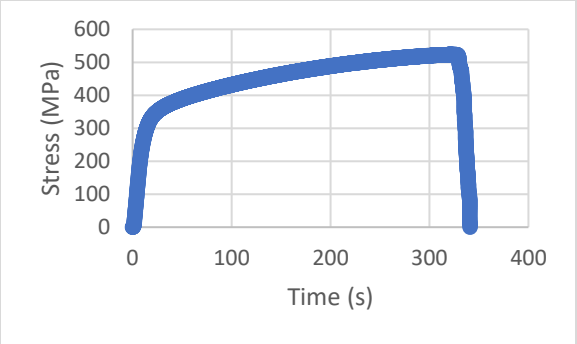

Figure 41: Stress vs Time of 21-Day Sample 8B

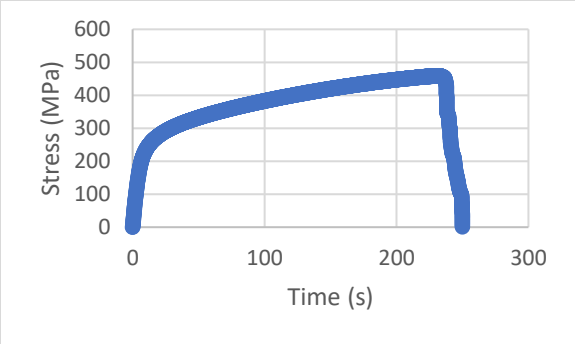

Figure 42: Stress vs Time of 21-Day Sample 3C

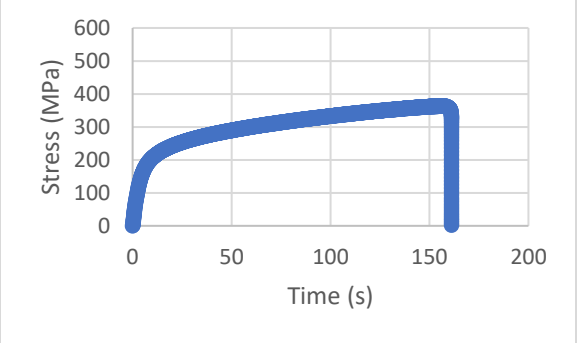

Figure 43: Stress vs Time of 21-Day Sample 5C

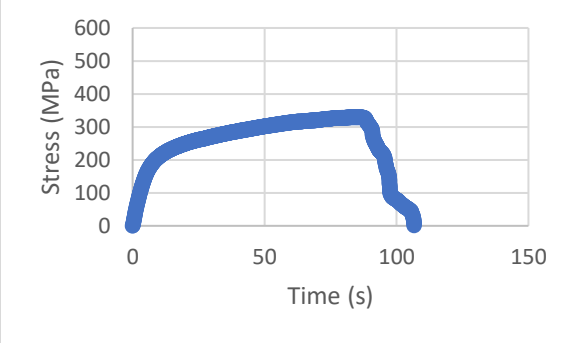

Figure 44: Stress vs Time of 21-Day Sample 2D

Figure 44 depicts sample 2D undergoing a brittle fracture for the same reason as sample 11C.

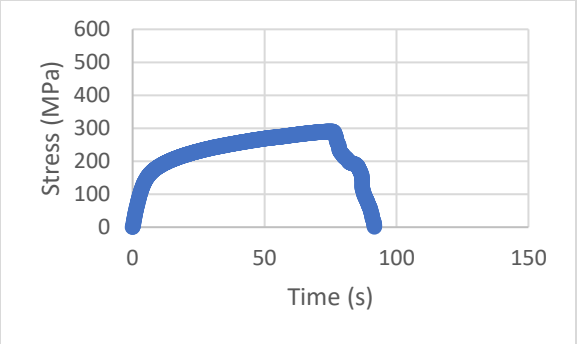

Figure 45: Stress vs Time of 21-Day Sample 5D

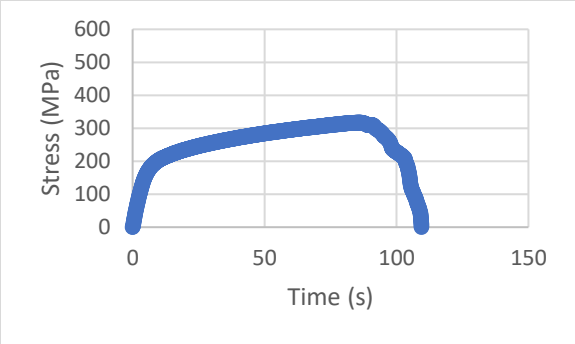

Figure 46: Stress vs Time of 21-Day Sample 9D

Both Figures 45 and 46 depict brittle fractures of samples 5D and 9D respectively. All of sample group D's specimens for 21-days fractured early in a brittle manner.

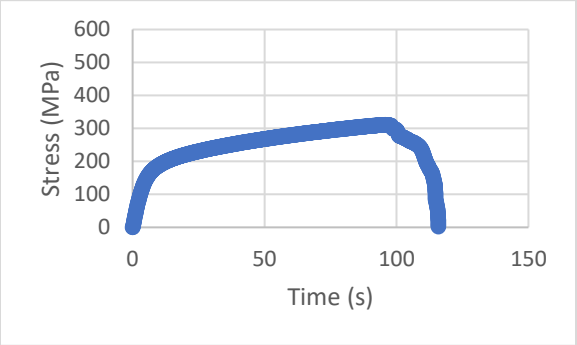

Figure 47: Stress vs Time of 43.5-Day Sample 2A

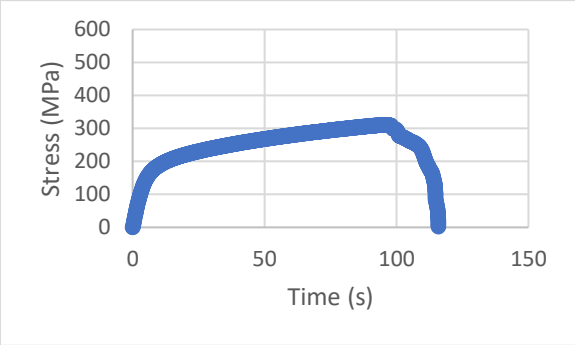

Figure 48: Stress vs Time of 43.5-Day Sample 5A

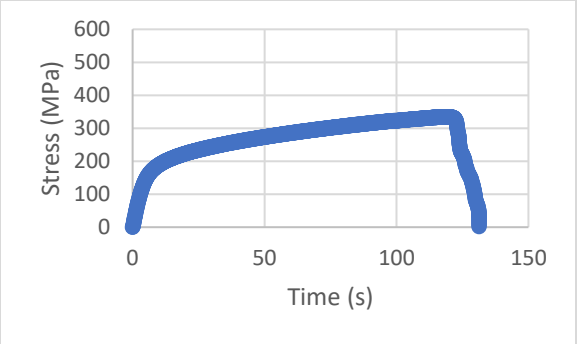

Figure 49: Stress vs Time of 43.5-Day Sample 8A

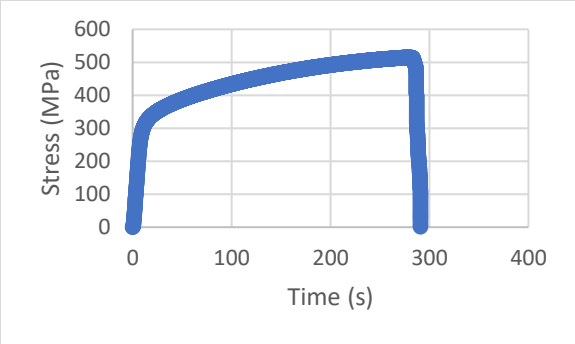

Figure 50: Stress vs Time of 43.5-Day Sample 4B

Of the 43.5-day samples, Figure 50 showing sample 4B is the only specimen to display characteristics of a ductile fracture. Figures 47 through 56 all show brittle fractures with the exception of Figure 50.

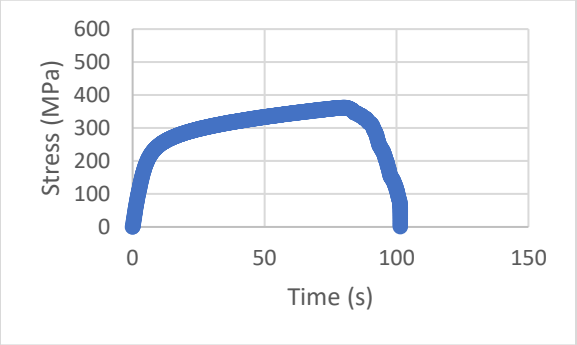

Figure 51: Stress vs Time of 43.5-Day Sample 9B

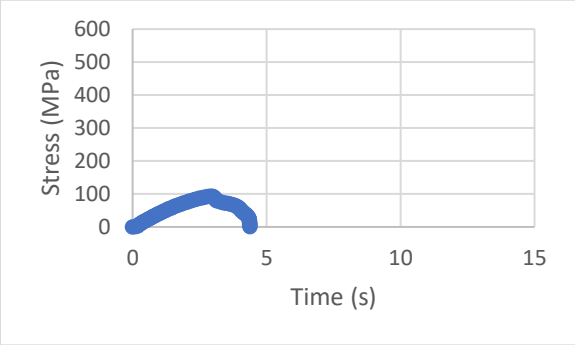

Figure 52: Stress vs Time of 43.5-Day Sample 4C

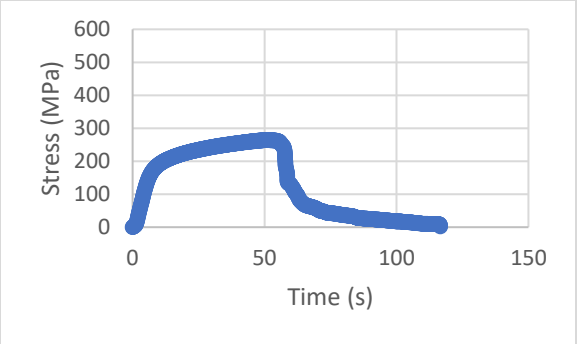

Figure 53: Stress vs Time of 43.5-Day Sample 8C

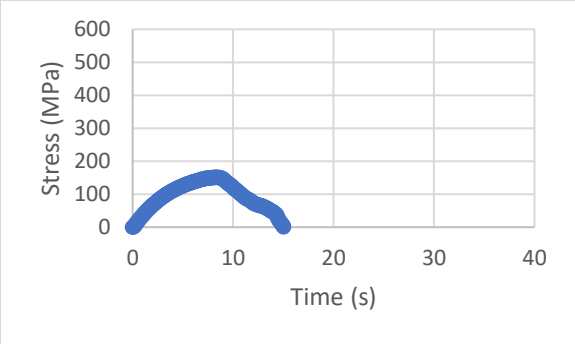

Figure 54: Stress vs Time of 43.5-Day Sample 3D

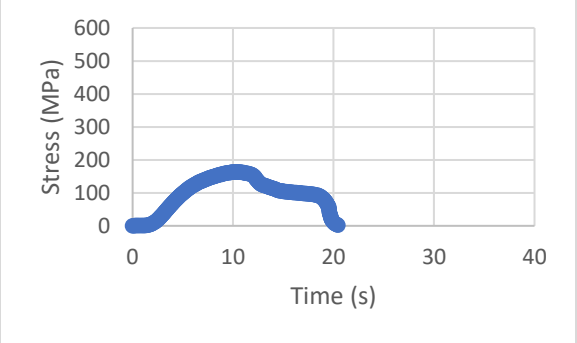

Figure 55: Stress vs Time of 43.5-Day Sample 6D

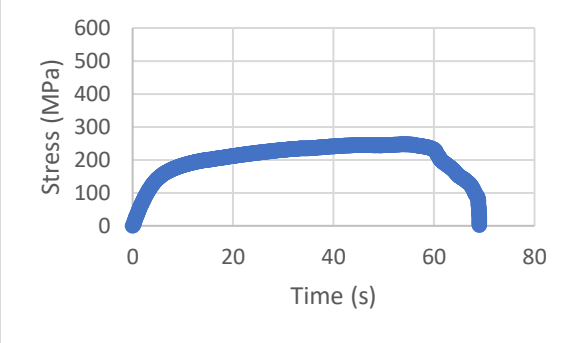

Figure 56: Stress vs Time of 43.5-Day Sample 8D

To better illustrate why it was chosen to display only the stress versus time curves rather than the stress versus strain, Figure 57 will compare the two different graphs for the control sample 4D below.

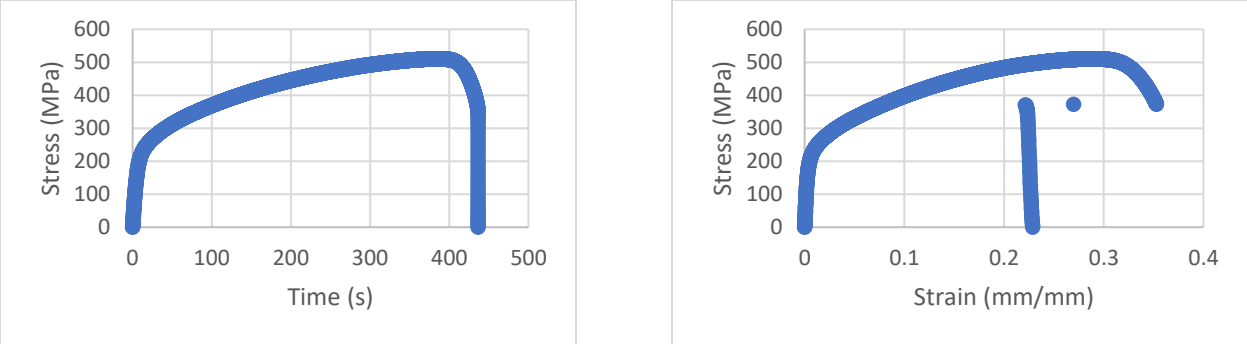

Figure 57: Comparison of the Stress vs Time Graph and the Stress vs Strain Graph of Control Sample 4D

From Figure 57, one can see that the fracture is exhibiting some ductile behavior, with the small decrease in slope before the vertical drop indicating failure, using the stress versus time curve, but it is not clear if only referring to the stress versus strain curve.

To view all of the samples' stress-strain curves, with data removed after the fracture, refer to the Appendix.

Figures 25 through 57 have the stress axis formatted such that the range is from 0 to 600 MPa; this was done so that amplitude of each stress-time curve can be compared. The range of the X-axis on each curve was set to whatever best contains the data for the chart for visibility.

Unlike the weight-loss data, it is very difficult to see each individual sample when plotted on the same chart; this is for the same reason as why the time-axis was not fixed. For comparison of the ultimate tensile strength, yield strength, and young's modulus, it is best to refer to Figures 19 through 24.

The following Figures depicts the top-half of the fracture location of each tensile-elongation sample. All the images were taken at 100x magnification with glare-removal enabled. The important features to note are the smooth regions versus the pitted areas at the borders of the

corroded samples. The sections being viewed take place within the gauge-length of each tensile sample.

Figure 58: Top-Half Fracture of Control Sample TA Taken at 100x Magnification

The center of TA shows signs of some internal stress with the visible cracks. There is a large gouge-like region in the top-left of the image that is not homogeneous with the rest of the cross-section. There are no signs of pitting corrosion. Some distortion occurred during elongation. The fracture was ductile as per Figure 29.

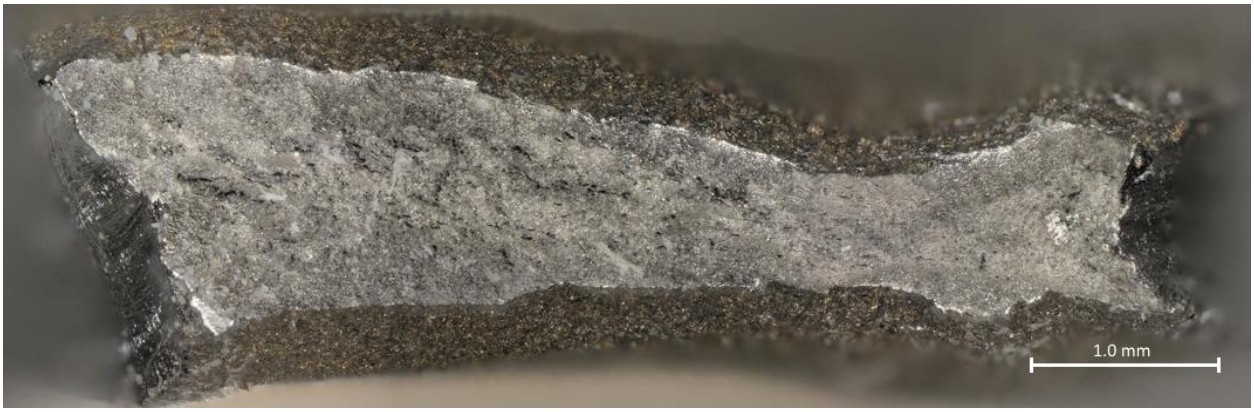

Figure 59: Top-Half Fracture of Control Sample 3A Taken at 100x Magnification

3A shows a significant amount of distortion before breaking. There are no obvious signs of corrosion. Some internal cracking is visible. 3A experienced a ductile fracture as per Figure 25 and can be seen by the narrowing of the edges.

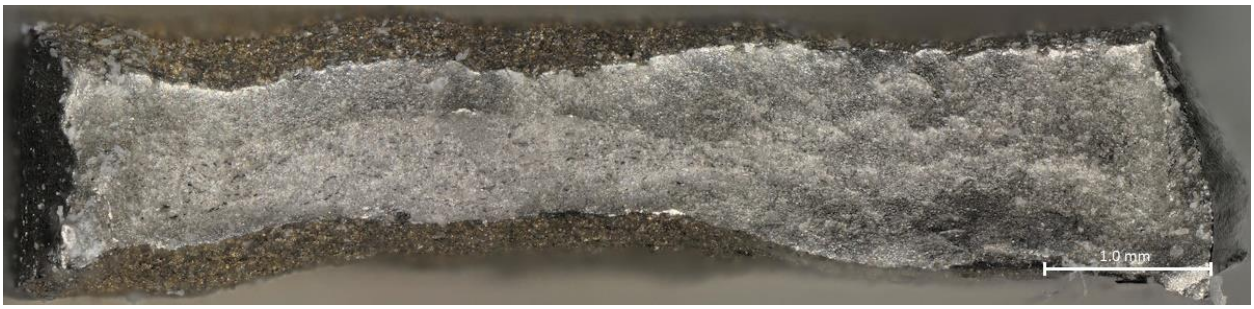

Figure 60: Top-Half Fracture of Control Sample 6A Taken at 100x Magnification

6A shows distortion in the cross-section prior to breaking. There are no signs of corrosion nor cracking in the sample. The fracture of 6A was ductile as per the fracture point of Figure 26.

Figure 61: Top-Half Fracture of Control Sample 7A Taken at 100x Magnification

7A shows distortion in the fracture. No cracks or sign of corrosion pitting is evident. 7A broke in a manner consistent with a ductile fracture as evidenced by Figure 27.

Figure 62: Top-Half Fracture of Control Sample BA Taken at 100x Magnification

BA shows distortion in the cross-section. The break shows homogeneous material; no signs of corrosion or pitting. The fracture of BA is best described as ductile using Figure 28 as reference.

Figure 63: Top-Half Fracture of Control Sample 5B Taken at 100x Magnification

5B exhibits some distortion in the cross section. Attention can be drawn to the cylindrical void present in the left-side of the image. There were several of these surface imperfections present in 5B, this one served as a stress-point for failure to occur at under load. The fracture of 5B was mostly ductile, although some brittle nature was observed as per Figure 30. See Figure 64 for an optical view of 5B's back with the void circled in red.

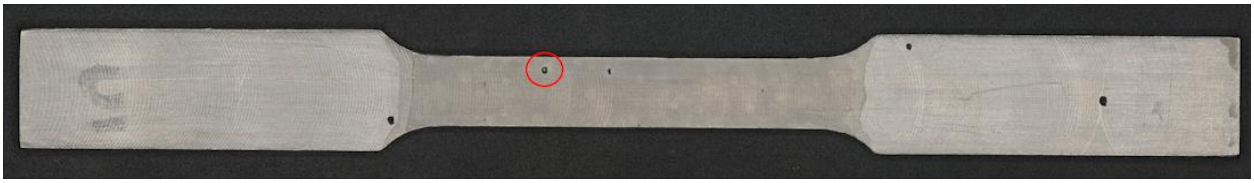

Figure 64: Optical Surface View of 5B's Back Featuring the Tensile Failure Location Circled in Red

Figure 65: Top-Half Fracture of Control Sample 10B Taken at 100x Magnification

10B shows some distortion in the cross-section. There are signs of cracking internally on the left-side of Figure 65. A Surface imperfection can be seen towards the top-middle of the image. 10B broke in a ductile manner according to Figure 31.

Figure 66: Top-Half Fracture of Control Sample 11C Taken at a Magnification of 100x

11C shows some distortion in the cross-section. Two main features are prevalent in the fracture of 11C: The topographical elevation difference between the left and the right sides and

the void to the right of the sample that allowed for some visible corrosion to occur. Note that the control samples did receive 16.7 hours of corrosion due to a mistake. This void and the small exposure to the corrosive environment allowed for the formation of ferrous oxide within the sample. 11C demonstrated a brittle fracture according to Figure 32. Figures 67 depicts the surface pit of 11C prior to being tensile-tested taken at 160x magnification.

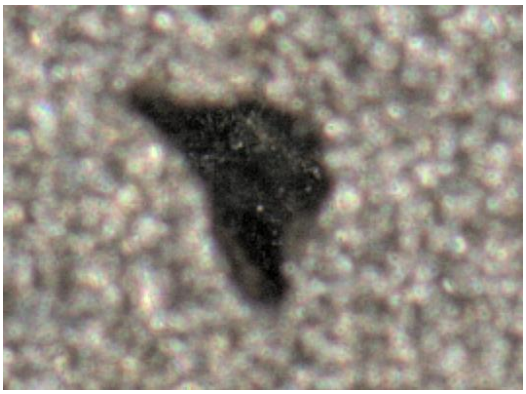

Figure 67: Optical Surface Image of Control Sample 11C's Front taken at 160x Magnification

Figure 67 shows that the feature from Figure 66 was visible prior to tensile-testing. It served as a stress-point for the fracture to occur at. A 3D scan was taken of Figure 67, but the unit incorrectly labeled the feature as convex rather than concave.

Figure 68: Top-Half Fracture of Control Sample 1D Taken at a Magnification of 100x

1D shows some distortion at the fracture location. Interestingly, there is substantial evidence of pitting corrosion towards the borders of the sample. The fracture of 1D is mostly

ductile as per Figure 33's fracture point. This is visible on the back-side of the sample prior to being tensile tested. The corrosion is seen as a duller, darker gray, coming in from the edges, with visible dark-spots present. When corrosion ends, the metal becomes lighter and shiny, with minimal to no dark inclusions. In this image, one can see the corrosion features going around the entire sample, although there is more surface penetrate on the top of the image. Since this is a control, this bit of corrosion is due to the accidental exposure for 16.7 hours. See both an optical view of 1D's back as well as a height-mapped version of Figure 68 in Figures 69 and 70.

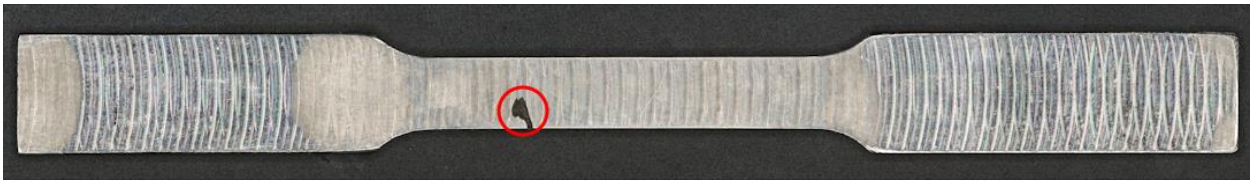

Figure 69: Optical Back Image of 1D Depicting a Surface Pit with a Red Circle

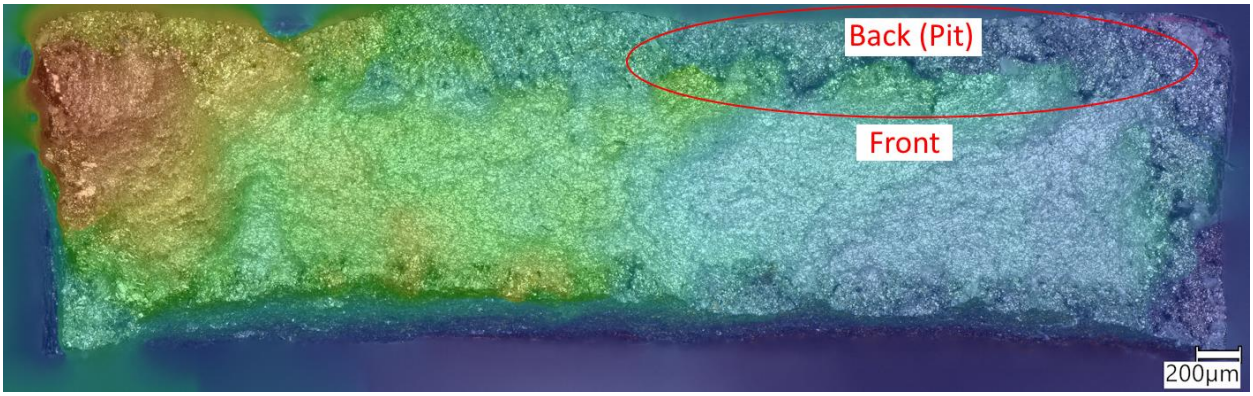

Figure 70: Topographical Map of 1D showing the Pit in the top-right.

Note that the warmer colors (e.g. red, orange, yellow) in Figure 70 represents surface features that are closer to the camera than the regions shown in cooler colors (e.g. green, blue, purple).

Figure 71: Top-Half Fracture of Control Sample 4D Taken at a Magnification of 100x.

4D shows significant signs of distortion at the fracture location. There are some cracks visible within the section but no signs of corrosion. 4D exhibited ductile fracturing as per Figure 34.

Figure 72: Top-Half Fracture of Control Sample 7D Taken at a Magnification of 100x

7D shows quite a bit of distortion at the fracture location. There is a crack visible within the section on the right-side of the image. There are no notable signs of corrosion present in the image. The fracture of 7D was ductile as per Figure 35.

Figure 73: Top-Half Fracture of Control Sample 10D Taken at a Magnification of 100x

There are some signs of distortion in sample 10D. There are no visible cracks within the cross-section however one can see some evidence of corrosion towards the top-region of Figure 73. 10D experienced a ductile fracture as per Figure 36. As with Figure 68, corrosion is present as a darker grey region with black inclusions, specifically at the top of the sample, while no corrosion present is shown as bright, shiny metal.

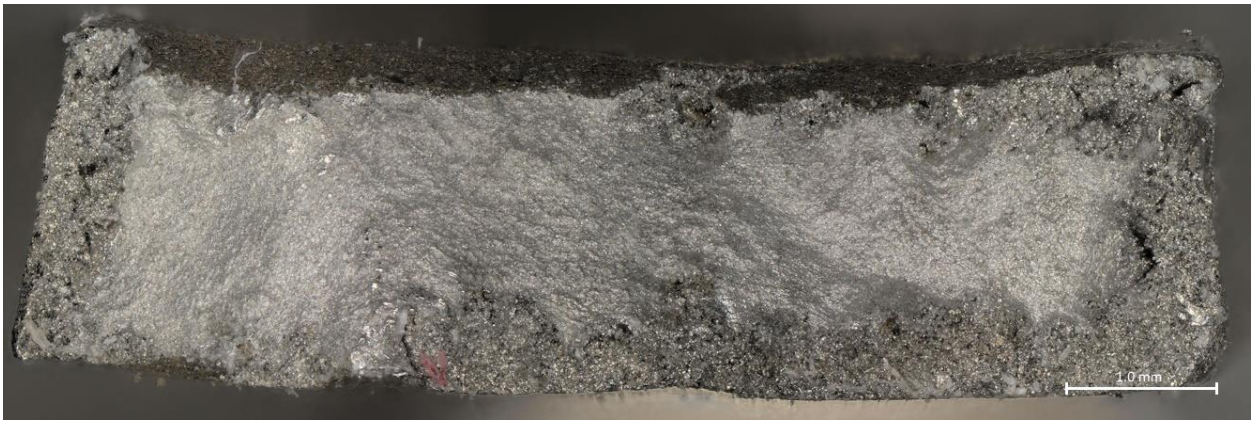

Figure 74: Top-Half Fracture of 21-Day Sample 1A Taken at a Magnification of 100x

1A shows some distortion in the cross-section. A notable amount of corrosion has occurred on the left and bottom-right portions of Figure 74, as indicated by the darker gray region with black inclusions. The fracture-point of Figure 37 depicts a ductile fracture.

Figure 75: Top-Half Fracture of 21-Day Sample 4A Taken at a Magnification of 100x

4A shows some distortion across the cross-section. Pitting corrosion can be observed along the entire border of the sample, as indicated by very dark holes throughout the top and bottom edges. The fracture of 4A according to Figure 38 is mostly ductile; due to the slope of the fracture point, there were likely some small regions that broke in a brittle manner.

Figure 76: Top-Half Fracture of 21-Day Sample 9A Taken at a Magnification of 100x

9A shows minor amounts of distortion throughout the fracture. There are no notable cracks within the pristine area of the section, but evidence of corrosion is present around the borders of the section. 9A broke in a mostly ductile manner as per Figure 39, but some regions of the fracture-point suggest it was not far from being brittle.

Figure 77: Top-Half Fracture of 21-Day Sample 3B Taken at a Magnification of 100x

3B shows a moderate amount of distortion throughout the fracture. There are some small internal cracks within the left and right portions of the image. Very minor amounts of pitting corrosion can be seen, most notably at the extreme left-side of Figure 77. 3B exhibited classic ductile fracturing as the border of the section obviously shows the "cup" feature raised to the viewer as well as Figure 40.

Figure 78: Top-Half Fracture of 21-Day Sample 8B Taken at a Magnification of 100x

8B shows very little distortion at all across the fracture site. There are no significant cracks internally, and very little evidence of pitting corrosion. The corrosion that is present is only visible in the top-right corner of Figure 78. Figure 41 suggestes that the fracture of 8B was mostly ductile.

Figure 79: Top-Half Fracture of 21-Day Sample 3C Taken at a Magnification of 100x

3C shows moderate signs of distortion. There is very prevalent pitting corrosion occuring around the border of the sample. Figure 43.5 shows that the fracture of 3C is best described as ductile. Most notably, there is a surface defect on the back-side of the sample at the fracture location visible in the cross-section in the top-middle region of Figure 79. Figure 80 and Figure 81 depict both a surface view as well as a 3D scan of the pit.

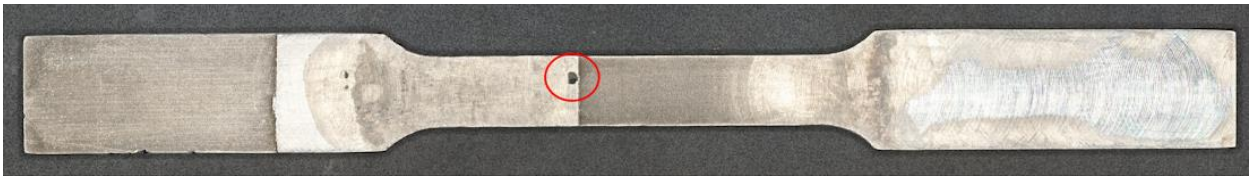

Figure 80: Optical Surface image of 3C's Back with Surface Pit Circled in Red

3C fractured directly across the red circled region in Figure 80. This area can be seen in Figure 79. Figure 81 shows a 3D scan taken of the location at 100x.

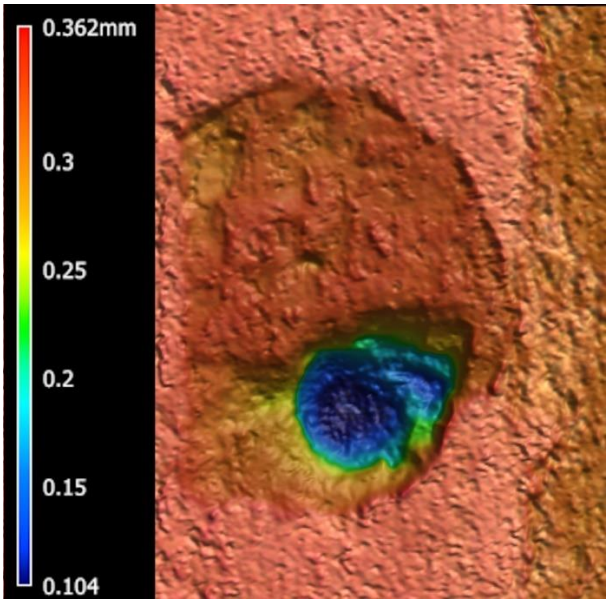

Figure 81: 3D-Rendered Pit of 3C's Back Before Tensile-Testing

Figure 81 to the left and Figure 80 depict the surface defect that became a point of stress where 3C ultimately fractured during tensile-testing. Regarding the scale shown in Figure 81, one can see that the pit is approximately 0.258 mm in depth. 3C's actual thickness measurement was recorded as 1.57 mm. The pit propagated 16.4% through the thicknesss of 21-Day Sample 3C which looks reasonable referring to Figure 79.

Figure 82: Top-Half Fracture of 21-Day Sample 5C Taken at a Magnification of 100x

5C shows mild amounts of distortion across the cross-section. It shows severe pitting corrosion around the border of the section, with large changes in the color of the metal on both the top and bottom of the figure. Figure 43 depicts a mostly ductile fracture based on the fracture-point.

Figure 83: Top-Half Fracture of 21-Day Sample 2D Taken at a Magnification of 100x

2D shows some distortion across the cross-section. There is substantial evidence of pitting corrosion across the borders of the sample. When looking at this figure, the corrosion is identified as dark, dull gray, with some brownish spots indicating potential rust within the surface. It also appears to be more porous showing plenty of pits. It has the appearance that it is ready to crumble apart, although the sample held together all the way until it tensile-elongation tested. The fracture of 2D took place in steps, that is it was not ductile, rather brittle. Figure 84 below depicts a topographical map of 2D's fracture.

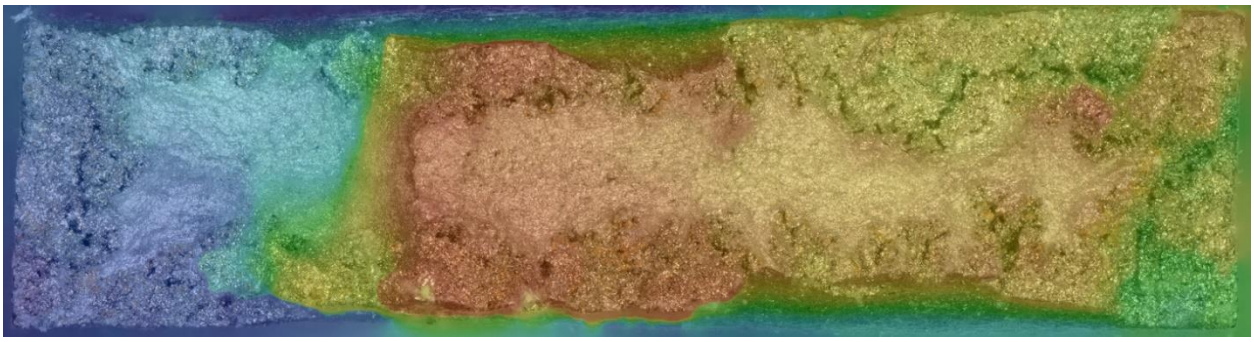

Figure 84: Topographical Representation of Figure 81

It can be seen that there are three separate regions in the fracture-site of 2D; this is evident by the three separate colors blue, red, and yellow. The fracture was brittle evident by both Figure 84 as well as Figure 44's fracture point at around 90 seconds.

Figure 85: Top-Half Fracture of 21-Day Sample 5D Taken at a Magnification of 100x

5D shows minor distortion across the fracture location. It has substantial pitting from corrosion throughout the border of the sample. It has the same crumbly appearance as seen in Figure 84 The fracture of 5D was brittle as evidenced by Figure 45's fracture point.

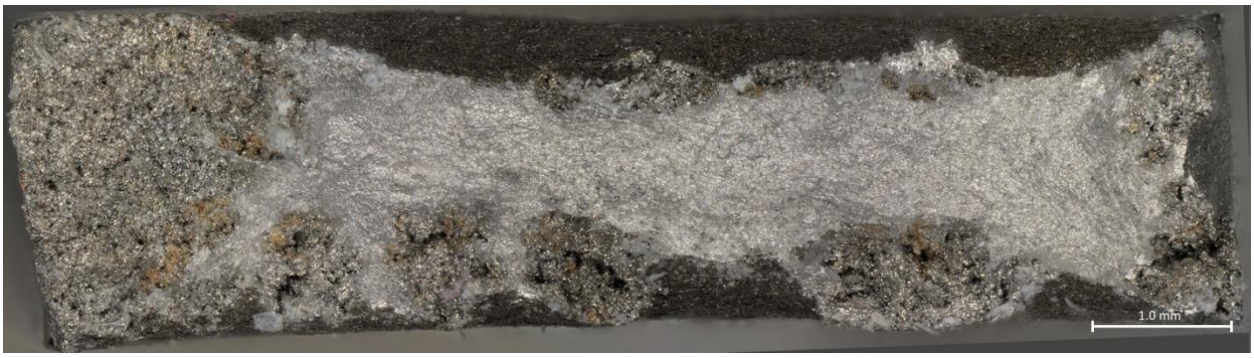

Figure 86: Top-Half Fracture of 21-Day Sample 9D Taken at a Magnification of 100x

9D shows moderate distortion across the cross-section. Substantial corrosion is present especially on the left-side of Figure 86, with the same crumbly appearance as Figures 84 and 85. The fracture was brittle as evidenced by Figure 46's fracture point.

Figure 87: Top-Half Fracture of 43.5-Day Sample 2A Taken at a Magnification of 100x

2A shows little distortion across the cross-section. There is substantial evidence of pitting corrosion occurring along the border of the sample, with the dark, dull gray also beginning to penetrate into the lighter metal on the left side of the image. The fracture was brittle as evident by Figure 47's fracture point.

Figure 88: Top-Half Fracture of 43.5-Day Sample 5A Taken at a Magnification of 100x

5A shows very little distortion across the fracture location. There is a significant amount of pitting corrosion evident around the border of the cross-section. The fracture was brittle as supported by the fracture point depicted by Figure 48.

Figure 89: Top-Half Fracture of 43.5-Day Sample 8A Taken at a Magnification of 100x

Sample 8A shows minimal distortion across the cross-section. There is a substantial amount of corrosion evident around the perimeter of the sample, with large areas of pitting and void coalescence. The fracture of 8A was brittle as evident by Figure 49's fracture point.

Figure 90: Top-Half Fracture of 43.5-Day Sample 4B Taken at a Magnification of 100x

Sample 4B shows a moderate amount of distortion across the cross-section. There is a very large defect present in 4B in the right-most portion of Figure 90. A mild amount of pitting corrosion can be seen around the borders of 4B. There are some small cracks present in the pristine area of the section. Unlike the rest of the 43.5-Day Samples, 4B demonstrates a ductile fracture as evident by Figure 50's fracture point.

Throughout the corrosion of 4B, a location near the neck of the sample progressively thinned out during the duration of the corrosion, as shown in Figure 91: a 3D-scanned timeline of

4B’s corrosion by time-stamp.

Figure 91: Chronological Progression of 4B’s Corrosion Depicted by 3D Topographical Scans

4B’s fracture location was along the gauge-length towards the transition region approaching the labeled, thicker area of the tensile sample (i.e. the right side of Figure 91 where the neck became thinner with increasing corrosion duration). It can be seen that this region was not prevalent at the start of the experiment, but grew into a point of stress where the sample would ultimately fail under load.

4B’s fracture is receiving additional notes due to its excellent tensile elongation properties as seen in Figure 50, in direct contrast to the rest of the 43.5-day samples which performed poorly. It was checked to ensure that the tensile data was not mismatched.

Figure 92: Top-Half Fracture of 43.5-Day Sample 9B Taken at a Magnification of 100x

9B showed almost no distortion across the cross-section. There is substantial pitting corrosion around the border of the sample. There is a very large defect in the bottom-right side of Figure 92 that also appears on the front-side of 9B's surface scans. This pit served as a stress-point where failure eventually occurred in a brittle-manner under load according to Figure 51. Figure 93 shows an optical view of the front-side of sample 9B at the start and end of the corrosion experiment, with the defect where the sample failed also showing in the top-right side of the gauge length.

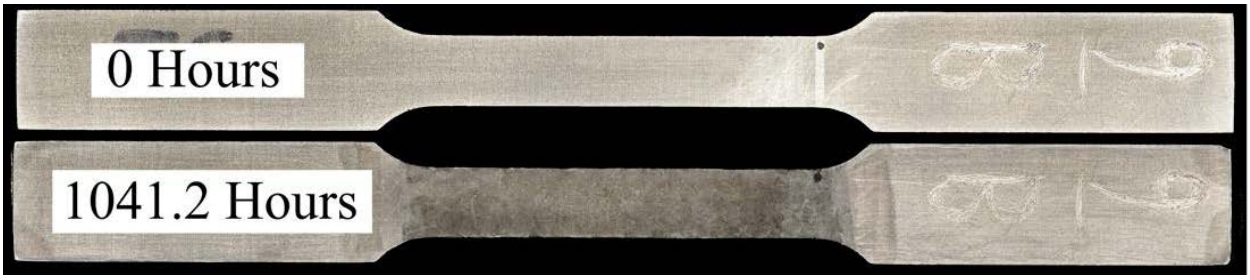

Figure 93: Comparison of 9B's Front Pit at the Neck of the Sample at the Start and End of the Experiment.

Figure 93 shows that the width of the defect on 9B did not substantially change throughout the corrosion. It is unknown what the original depth of the pit started at, but a close-up 3D scan was taken of the surface defect before tensile testing the sample, as shown in Figure

94.

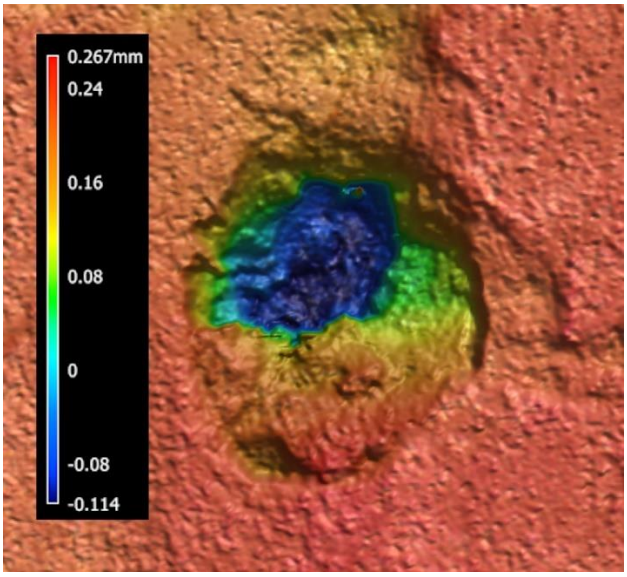

Figure 94: 3D Topographical Scan of 9B's Front Pit Taken at 160x Magnification

Figure 94 depicts the defect as being approximately 0.381 mm deep based on the color scale. This puts it at around a quarter of the overall depth of sample 9B. When referencing Figure 92, this estimate seems to be shallower than what one would expect; Figure 92 shows the defect reaching 50% of the sample's overall depth. This defect was created as a void during the printing of the sample

Figure 95: Top-Half Fracture of 43.5-Day Sample 4C Taken at a Magnification of 100x

Sample 4C shows almost the entirety of the fracture-surface that has been corroded by pitting. There is no distortion of the sample at all. The sample was completely brittle when broken as evidenced by Figure 52's fracture point. A contrast of 4C at 0 hours of corrosion versus at 800.8 hours of corrosion can be seen in Figure 96.

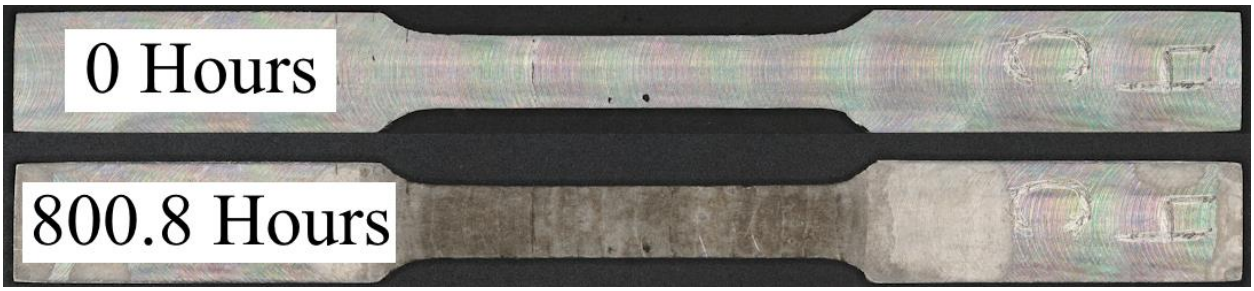

Figure 96: Comparison of 4C's Front at a Corrosion Time of 0 Hours Versus 800.8 Hours

The most prevalent features one notices when comparing 4C at 0 hours versus 800.8 hours is how much darker 800.8 hours is along the gauge-length and the vertical lines that start forming at the edges of the sample due to corrosive attack. The two surface defects remain mostly unchanged throughout the course of the experiment.

Figure 97: Top-Half Fracture of 43.5-Days Sample 8C Taken at a Magnification of 100x

8C shows very little distortion across the sample. Almost the entire cross-section has been affected by pitting-corrosion. A narrow region near the center of the fracture is still uncorroded metal. The fracture of 8C was brittle as seen by the fracture point of Figure 53.

Figure 98: Top-Half Fracture of 43.5-Day Sample 3D Taken at a Magnification of 100x

3D shows essentially no distortion across the cross-section. There entire surface shows evidence of pitting corrosion with just a few very small regions, directly in the center of the sample, with the original metal appearance. The fracture was completely brittle as per Figure 54's fracture point.

Figure 99: Top-Half Fracture of 43.5-Day Sample 6D Taken at a Magnification of 100x

6D as almost no distortion to it. The pitting corrosion has affected almost the entire cross-section of the sample, with only a tiny amount of the original metal in the center-top of the image. The fracture of 6D was brittle as shown by Figure 55's fracture point.

Figure 100: Top-Half Fracture of 43.5-Day Sample 8D Taken at a Magnification of 100x

8D has very little distortion across the fracture surface. Pitting corrosion can be seen across the vast-majority of the cross-section. A moderate patch of pristine steel exists from the middle to right-portion of Figure 100, while the left-side of the image has the standard crumbly appearance. The fracture point of Figure 56 shows that the break of 8D was brittle in nature.

A summary of the type of fracture of all 32 samples is listed in Table 7. The fracture type was determined by looking at the fracture-point of the stress versus time curve. Note that the

classification of each sample is subjective; some of the borderline samples were called ductile despite not having a perfectly vertical break at the fracture point of the stress versus time curve.

Table 7: Type of Tensile Fracture by Sample Name

Sample Code	HCl Immersion Duration	Fracture Type	Sample Code	HCl Immersion Duration	Fracture Type
TA	Control	Ductile	10B	Control	Ductile
1A	21 Days	Ductile	3C	21 Days	Ductile
2A	43.5 Days	Brittle	4C	43.5 Days	Brittle
3A	Control	Ductile	5C	21 Days	Ductile
4A	21 Days	Ductile	8C	43.5 Days	Brittle
5A	43.5 Days	Brittle	11C	Control	Brittle
6A	Control	Ductile	1D	Control	Ductile
7A	Control	Ductile	2D	21 Days	Brittle
8A	43.5 Days	Brittle	3D	43.5 Days	Brittle
9A	21 Days	Ductile	4D	Control	Ductile
BA	Control	Ductile	5D	21 Days	Brittle
3B	21 Days	Ductile	6D	43.5 Days	Brittle
4B	43.5 Days	Ductile	7D	Control	Ductile
5B	Control	Ductile	8D	43.5 Days	Brittle
8B	21 Days	Ductile	9D	21 Days	Brittle
9B	43.5 Days	Brittle	10D	Control	Ductile

From Table 7, one can see all samples labeled according to their corrosion duration as well as the fracture type they were classified as. One may notice that every 43.5-day corrosion sample exhibited a brittle fracture with the exception of 4B, which was an anomaly. All of the 21-day samples had a ductile break except for the sample-group D. All of the control samples were ductile except for 11C.

Chapter 4: Discussion

In order to determine which build-orientation was the best for the Mazak VC-500/5X AM HWD in terms of corrosion-resistance, it is necessary to revisit the data obtained from both the

tensile-elongation testing and the weight-loss data. The first section will be a discussion of the weight-loss data, then the tensile-elongation, followed by an overall look-at-both before ranking the samples.

4.1 Mass-Loss

In terms of weight-loss the best method to compare one sample to another is to evaluate each group's performance as indicated by the normalized weight-loss data. This gives all samples an equal starting value and accounts for samples having slightly different dimensions. The most important data to consider when evaluating these Figures 15, 16, and 17 is the relative ranking of sample groups going in ascending order of total mass lost, or descending total mass. For manufactured parts in general, it is undesirable for a part to lose mass in a corrosive environment. Therefore, all one must do is rank samples that lose the least amount of mass better than those that corrode more severely.

In general, the order of samples in increasing normalized mass-loss does not fluctuate much as the corrosion duration increases. For this reason, Table 8 lists the final normalized mass-loss for each sample taken at the maximum corrosion duration available; that is 507.8 hours for 21-day samples, 1041.2 hours for 43.5-day samples, and the date 1/23/2024 for the control samples. Table 8 summarizes the most important information from Figures 15, 16, and 17.

Table 8: Ranking Each Sample by Corrosion Duration and Descending Normalized Mass

	Control		21-Day		43.5-Day	
Rank within Corrosion Group	Sample Code	Final Normalized Mass	Sample Code	Final Normalized Mass	Sample Code	Final Normalized Mass
1	5B	0.9998	1A	0.9970	8A	0.9911
2	11C	0.9997	4A	0.9969	5A	0.9905
3	10B	0.9997	9A	0.9968	2A	0.9895
4	TA	0.9996	9D	0.9964	3D	0.9886
5	BA	0.9996	2D	0.9962	8D	0.9881
6	7A	0.9995	3B	0.9961	6D	0.9878
7	3A	0.9995	5D	0.9957	4B	0.9816
8	7D	0.9995	8B	0.9946	9B	0.9744
9	4D	0.9995	3C	0.9940	8C	0.9703
10	6A	0.9994	5C	0.9896	4C	0.9637
11	10D	0.9988				
12	1D	0.9985				

Look at the columns for the 21-day corrosion data as well as 43.5-day from Table 8. One can see that the order of the sample groups in descending order of normalized mass is A, D, B, and C. The control group can be mostly disregarded as there is no corrosion present, besides 16.7 hours, to influence the ranking. Sample group A in the presence of a corrosive 1.0 M HCl environment maintained its mass better than the other groups. Group D performed better than group B. All groups did better than group C.

One would expect that the normalized mass-lost would directly correlate to how deep

pitting corrosion manifested itself within the cross-section of the fracture site such as Figures 95 and 97, samples 4C and 8C, that have both substantial mass-loss as well as heavy-pitting in the cross-section. However, this is not always the case. When comparing Figures 90 and 92 to Figures 87 through 89, one would expect sample group B to show less normalized mass-loss versus sample group A. This intuition is formed by visually comparing the total area of the shiny, pristine metal to the dark and pitted metal that has been affected by corrosion.

Figure 101: Fracture of 2A with the Pristine Regions Highlighted Yellow Versus the Corroded Regions Highlighted Red

Figure 101 is an edit of Figure 87 that depicts the regions that are corroded versus the areas that have been unaffected, or pristine, for sample 2A. Consider the fraction of the pristine, highlighted-yellow region, as compared to that of the entire fracture surface, a summation of the red and yellow regions. It would be expected that samples that have lost a greater mass would have a smaller region of yellow in comparison to the total area of red and yellow.

However, Figures 90 and 92 from sample group B show a smaller fraction of corroded cross-section area to that of Figures 87 through 89, the sample group A. This can occur in a couple of ways. It could be that the cross-sectional area of pristine versus corroded regions changes across the length of the sample and that the fracture point did not capture the highest

areas of corrosion. It could also be that the mass loss of sample group B was largely due to the voids or inclusions visible in both the fracture locations. Both samples from the 43.5-day corrosion group from B possessed these section defects. Figure 102 below shows the fracture-site of 4B, but with the pristine and corroded portions highlighted in yellow and red, similar to Figure 101.

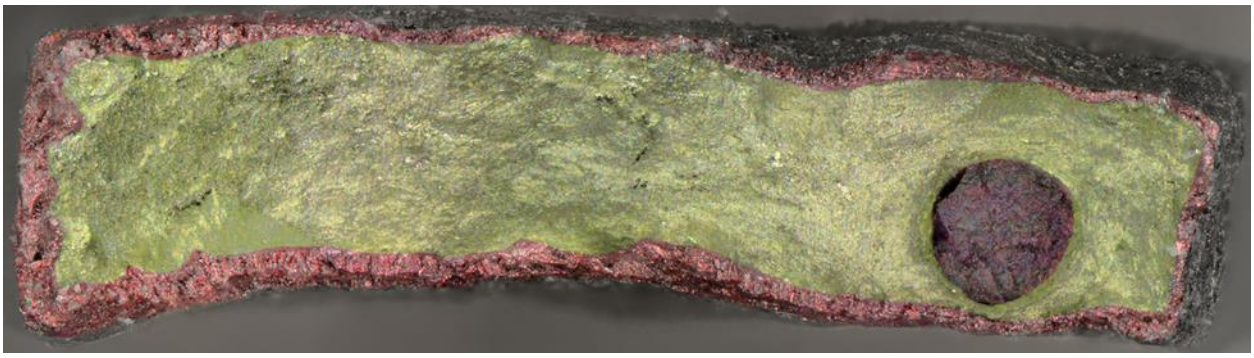

Figure 102: 43.5-Day Sample 4B shown with Pristine Metal Highlighted in Yellow and Corroded Metal Highlighted in Red

When comparing Figures 101 and 102, the aforementioned large difference in corroded area can be seen. 4B shows substantially less corrosion at the fracture-site than 2A, despite both being samples corroded for 1041.2 hours.

Even in the 21-day category, sample B also had a greater fraction of pristine area versus corroded, yet Table 8 shows that sample group B underwent greater amount of mass-loss than group A. Group B may have had other inclusions and voids present within the sample that allowed for this mass loss to occur more readily, that are not visible in the fracture surface as it occurred in other locations within the samples.

Regardless of this curious phenomenon, the best build-orientations in terms of mass-loss are Unidirectional 90° (A), Bidirectional 0-90° (D), Unidirectional 0° (B), and lastly

Bidirectional 0-45° (C). This behavior corresponds with porosity and tensile strength obtained from control samples from these various builds. From testing samples built by the Mazak VC-500/5X AM HWD, it was determined that the build direction played a large role in the behavior of the samples. If the print-head moved from front to back or back to front, 90°, minimal porosity was formed. If the print-head moved side-to-side, 0°, less porosity was formed if the print-head moved from right-to-left than if the print-head moved left-to-right, where porosity was substantial. If the print-head moved in the 45° direction, heavy porosity occurred within the samples.

Given that samples that were built in the direction of 90° are less porous than those built in the 0° or 45°, it makes sense that group A would perform better than groups B, C, and D since it was unidirectionally printed in the 90° direction. Since sample group B was printed unidirectionally 0° specifically from right-to-left, the ideal direction for 0°, it makes sense that it also performed well, but not as well as unidirectional 90°. Bidirectional 0-90°, group D, contains the best print direction, 90°, but it also contains the poor print-direction of 0° left-to-right. This caused it to perform worse than group A, but slightly better than group B. Bidirectional 0-45°, group C, only contained one print-direction that was not considered bad: 0° right-to-left. The other possible directions, 0° left-to-right and both of the 45° directions were known to have poor porosity.

This suggests that SS316L builds containing 90° print-direction on the Mazak VC-500/5X AM HWD are better for maintaining mass under corrosion than builds printed in the 0° or 45° direction. Unidirectional may have performed marginally better than bidirectional, but this is because bidirectional contains the print-directions that are known to have higher porosity. Bidirectional 0-45° (C) performed poorly in comparison to groups A and D.

4.2 Tensile-Elongation

The second point of discussion to evaluate the performance of all four different build-orientations is the tensile-elongation mechanical properties. Figures 22, 23, and 24 depict the ultimate tensile strength, yield strength, and Young's modulus and are summarized in Tables 9, 10, and 11.

For a manufactured SS316L part, it is generally desirable to have as high of an ultimate tensile strength possible. Therefore, each of the sample groups will be ranked by looking at the overall decrease in ultimate tensile strength using the mean minus one standard deviation as the measured point for each corrosion group. The standard-deviation is considered in this analysis because of the small-sample size of this experiment as well as the relatively large variance observed in some groups among the tensile-elongation measurements. The aim is to display a pseudo worst-case scenario for each group. Table 9 depicts the mean minus one standard-deviation for the ultimate tensile strength among the sample groups. Table 9 was constructed from Figure 22 in order to help rank each sample group per the ultimate tensile strength.

Table 9: Mean Minus One Standard-Deviation for Ultimate Tensile Strength for each Sample Group in MPa

Sample Group	Control	21-Day	43.5-Day
A	464.5	396.5	312.7
B	521.9	516.6	330.8
C	176.7	343.2	58.1
D	428.4	292.5	134.9

From table 9, it is seen that in order of descending ultimate tensile strength the control has the following order: B, A, D, and C. 21-day has the following order: B, A, C, and D. 43.5-day has the following order: B, A, D, and C.

Apart from the 21-day corrosion group, the order for both the control as well as the longest duration corrosion group for ultimate tensile strength from best to worst is Unidirectional 0° (B), Unidirectional 90° (A), Bidirectional 0-90° (D), and lastly Bidirectional 0-45° (C). For ultimate tensile strength, it appears that unidirectional printing plays the biggest role. This is for reasons as discussed in the mass-loss evaluation; the bidirectional printing directions contain both the optimal as well as the highly porous print-directions so it makes sense that unidirectional 0° would perform better than bidirectional 0-90° as group B already outperformed group A in terms of ultimate-tensile strength and both groups A and B do not contain the "bad" print-directions, whereas bidirectional 0-90° does.

This data does seem to contradict the mass-loss data, as build B lost more mass and exhibited more porosity than build A. Based on the mass-loss, there was potential that build B was printed in the worse left-to-right 0° direction, but the tensile properties seem to imply that build B was built with the better right-to-left 0° direction. An alternative hypothesis as to why group B contained pores could have been from the differences in the printer-parameters. Group B did have a slightly lower additive federate, twice the shielding gas flow, a slightly lower hot-wire power, and a higher layer-height. These parameters could have been more prone to porosity than the other builds.

The next tensile-elongation property to consider is yield-strength. The yield-strength for all of the samples was determined at a strain value of 0.2%. It is not always desired to have as high of a yield-strength as possible as it typically comes at a price. A well-known relationship

exists that tells us that as tensile strength increases, ductility tends to decrease. A SS316L part with a really high yield strength is not necessarily superior to a part demonstrating a lower yield strength. As yield strength increases, ultimate tensile strength generally decreases [18]. With this consideration in mind, consider Table 10 below. It is constructed using Figure 23 using the mean minus one standard deviation similar to Table 9.

Table 10: Mean Minus One Standard-Deviation for Yield Strength Evaluated at 0.2% Strain for each Sample Group in MPa

Sample Group	Control	21-Day	43.5-Day
A	113.8	244.5	213.7
B	130.6	148.8	163.2
C	57.1	94.1	58.8
D	84.7	107.6	90.5

From Table 10, one can construct a ranking in descending order for each corrosion group. From the control group, the order is: B, A, D, and C. For the 21-day group, the order is: A, B, D, and C. For the 43.5-day group, the order is: A, B, D, and C.

In terms of yield strength, the overall order in terms of highest to lowest sample groups is as follows: Unidirectional 90° (A), Unidirectional 0° (B), Bidirectional 0-90° (D), and lastly Bidirectional 0-45° (C). Similarly to the ultimate tensile strength, it appears that the samples printed using a unidirectional build-orientation had the best results in terms of yield-strength.

As a sample is exposed to a corrosive environment it becomes more brittle. This brittleness results in an increase of Young's Modulus. Depending on the amount of corrosion that occurred will determine where the yield strength of the sample will be when evaluated at a strain 0.2%. If there is a lower amount of corrosion, as in the case of groups A and B, then the increased slope in the elastic region of the stress-strain curve is going to shift the plastic region left-wards on the chart without significantly decreasing the ultimate tensile strength. Since strain is evaluated at 0.2%, this shift to the left demonstrates how it is possible to observe an increase in yield strength with increased corrosion. Sample groups C and D experienced a much greater amount of corrosion which substantially lowered the ultimate tensile strength of those two groups. The decrease for groups C and D were so severe that their ultimate tensile strength at 43.5 days were lower than their yield strengths as control samples. This is why groups C and D experienced almost no change in yield strength whereas groups A and B experienced an increase in yield strength.

The next characteristic to be evaluated from the tensile-elongation data is Young's Modulus. Being that Young's modulus is derived from the slope of the elastic region of a stress-strain curve, it is important to understand that a high value of Young's modulus implies a more rigid, stiffer part than one with a lower Young's modulus. Materials with a lower modulus of elasticity are more flexible.

The concern with parts undergoing corrosion is that they tend to become brittle. As a part becomes more brittle, the value of Young's modulus increases. Therefore, the ranking of each sample group will be based on ascending values of increases in Young's modulus. See Table 11 for the summary of Figure 24 where the value for each corrosion group is the mean minus one standard deviation.

Table 11: Mean Minus One Standard-Deviation for Young's Modulus for each Sample Group in GPa

Sample Group	Control	21-Day	43.5-Day
A	44.5	56.3	51.9
B	42.2	84.6	75.3
C	21	45.4	39.9
D	46	57.6	46.7

Taking the Young's Modulus from the 43.5-day corrosion duration group and dividing it by the control group, subtracting one from that quantity, and multiplying the answer by 100%, a percent-increase for each group can be reported from Table 11. That is $\left(\frac{A_{43.5}}{A_{Control}} - 1\right) * 100\%$. See Table 12 below for the resulting values of the aforementioned arithmetic.

Table 12: The Percent-Increase per Sample Group in Terms of Young's Modulus from the Control Group to the 43.5-Day Corrosion Group

Sample Group	Young's Modulus Percent Increase
A	16.6%
B	78.4%
C	90.0%
D	1.5%

In order of ascending percent-increase of Young's modulus from Table 12: Bidirectional 0-90° (D), Unidirectional 90° (A), Unidirectional 0° (B), and lastly Bidirectional 0-45° (C). It

appears that a printing direction of 90° was most influential for strongest performance regarding Young's Modulus.

Sample group D showed the smallest increase in the modulus of elasticity. This may be surprising at first considering how severe the propagation of pitting corrosion was in Figures 98, 99, and 100, but it is also useful to recall that sample group D was the only control group to demonstrate evidence of pitting corrosion with only 16.7 hours of exposure, as shown in Figures 68 and 73.

Again, the concern with an increase in Young's Modulus as corrosion duration increases is that the sample is becoming more rigid and inflexible, which can indicate it is becoming more brittle. It is undesirable for a metallic part to fail prematurely due to embrittlement from corrosion. For all builds, the likelihood of increasing porosity increases with increased corrosion duration. Since corrosion produces hydrogen, and a hydrogen ion can react in solution before it becomes hydrogen gas, there is a chance for the hydrogen ions to move through the metal and react with iron or carbon to form iron hydride or carbon hydride. These hydrides are incredibly brittle; as more hydrides are formed due to longer exposure time in the corrosive media, there is an increased chance of embrittlement that would result in a premature fracture during tensile-elongation testing

Build C, which shows the largest increase in Young's modulus, or the largest change towards brittle behavior, is explained by its poor mechanical properties and its high porosity from the build. The more porous the metal, the more opportunity exists for corrosive media to penetrate the sample and form hydrides that are very brittle.

One final evaluation of corrosion properties is subjective, but it is a qualitative inspection

of the fracture-sites for each of the sample groups. Using an analysis similar to that of Figure 101, as well as considering any defects identified within the samples, a ranking of the best to worst sample groups can be listed as follows: Unidirectional 90° (A), Unidirectional 0° (B), Bidirectional 0-45° (C), and lastly Bidirectional 0-90° (D). The samples being printed unidirectionally was the strongest contributor to the performance in the fracture-site evaluations.

Groups A and B were both better than groups C and D in terms of ratio of pristine area to overall cross-sectional area; however, the presence of voids and inclusions in sample group B is concerning and ultimately resulted in it being rated second-place to group A.

The appearance of the fracture-sites of sample group C and D were both poor compared to that of sample groups A and B. Although sample group D did show evidence of corrosion even on the control sample with only 16.7 hours of corrosion, group C contained a sample that managed to be 100% pitted. Sample group D was marginally better than group C, but both of the bidirectional builds performed poorly in the fracture-site evaluations.

4.3 Overall

With each of the sample groups evaluated based on their performance in mass-loss and tensile elongation, it is now possible to start ranking the samples based on their overall corrosion-resistance throughout this experiment.

To make the summary easier to see, Table 13 is provided to list the order of sample groups as they ranked in each corrosion property.

Table 13: The Ranking Order from Best (1) to Worst (4) for each Sample Group for each Corrosion Property

Corrosion Property	1st (Best)	2nd	3rd	4th (Worst)
Mass-Retention	A	D	B	C
Ultimate Tensile Strength	B	A	D	C
Yield Strength (0.2% Strain)	A	B	D	C
Young's Modulus Increase	D	A	B	C
Fracture Site Evaluation	A	B	D	C

From Table 13, it is clear that the weakest build orientation belongs to that of group C: Bidirectional 0-45°. The strongest-performing sample group is A: Unidirectional 90°. If one looks at Table 13 carefully, they can determine that the second-best performing group was B: Unidirectional 0°. This leaves sample group D, Bidirectional 0-90°, in third-place.

For those wishing for a quantitative measure of final placement, one can take the summation of each groups placement per property and rank them from lowest to highest; that is, the groups that most frequently score the best will be ranked the highest. See Table 14 for the scoring method just described.

Table 14: Overall Score for each Sample Group Based on the Rankings of Table 13

Sample Group	Ranking Score (Lower is Better)	Overall Rank
A	7	1
B	11	2
C	20	4
D	12	3

From Table 14, the overall ranking of each sample group is as follows: Unidirectional 90° (A), Unidirectional 0° (B), Bidirectional 0-90° (D), and lastly Bidirectional 0-45° (C).

The porosity and mechanical properties seen from the builds explains these ranking. The build that does not contain a 0° orientation, build A, was the best performing. The build that contains the 45° orientation, build C, was the worst performing. For build B, which was the second best, the build was only printed in one direction, and was likely printed from right-to-left, the better direction for the printer. The change in build parameters, specifically the lower wire feed rate and lower hot wire power, likely lead to some vaporization, producing round holes. Where these voids were not present, the metal was strongly melted together. For build D, which was the second worst, the build contained 90°, which was the best direction, but it also contained 0° printed in both the highly porous left-to-right 0° direction as well as the better right-to-left 0° direction. The “bad” portion of the 0° printing direction caused the build to contain more pores and overall reduce the mechanical properties of the samples.

Overall, based on the rating metrics defined, the most important build-orientation parameters from the Mazak VC-500/5X AM HWD for the tensile samples created for corrosion testing in a 1.0M HCl immersion bath are unidirectional printing followed by the printing-

direction of 90°.

Chapter 5: Concluding Remarks and Recommendations

5.1 Concluding Remarks

The goal of this experiment was to determine the best build-orientations as printed by the Mazak VC-500/5X AM HWD building regarding corrosion resistance among four different options: Unidirectional 90°, Unidirectional 0°, Bidirectional 0-45°, and Bidirectional 0-90°. The methods in which the different build-orientations were measured was by mass-loss and tensile-elongation destructive physical analysis.

Samples were in the form of ASTM E8M 6 mm wide subsize specimens cut to a thickness of approximately 1.6 mm. These samples were separated into different exposure groups to a 1.0 M HCl immersion bath consisting of none (control), 21-Days, and 43.5 days.

Each corrosion session was approximately one full week in length, 7 days. After each week of corrosion, the sample masses were recorded, surface profilometry performed, and prepared for the next week of immersion. Once the samples reached their designated length of corrosion, they were broken using a tensile-elongation testing unit.

The samples from each build-orientation and corrosion exposure duration were compared with respect to their mass-loss over time, ultimate tensile strength, yield strength, modulus of elasticity, as well as microscopy of the fractured cross-section. Table 15 summarizes the mass and mechanical properties of the sample groups over the course of the experiment.

Table 15: Summary of Measured Properties of each Sample Group from 0 Days Compared to 43.5 Days

Sample Group	Mass-Loss (% of total mass)	Ultimate Tensile Strength ($\bar{x}$-σ) (MPa)	Yield Strength ($\bar{x}$-σ) (MPa)	Young's Modulus (% Increase)
A	0.96%	312.7	213.7	16.60%
B	2.20%	330.8	163.2	78.40%
C	3.30%	58.1	58.8	90%
D	1.18%	134.9	90.5	1.50%

Upon comparing all the metrics for each of the sample groups, a final ranking order from best-performing to worst in terms of corrosion-resistance was determined as follows: Unidirectional 90° (A), Unidirectional 0° (B), Bidirectional 0-90° (D), and lastly Bidirectional 0-45° (C).

5.2 Recommendations

If additional time and resources allowed, there would be a couple of items that would have been beneficial to explore: sample size, additional build-orientations, grain-structure microscopy, and print-parameters.

The sample-size was one of the largest restrictions in this experiment. Having an asymmetric number of samples available for each build-orientation in such few quantities lead to large standard-deviations when reviewing summaries of data within each corrosion metric. Having at least five samples available within each corrosion duration group per sample group would have made spotting outlier data much easier as well as shrink the standard-deviation. The availability of samples in this experiment was determined by what was left-over from previous testing.

An opportunity to better determine the optimal build-parameters for key-corrosion

properties would be available with a deeper analysis of build-orientations. In this experiment, unidirectional 90°, unidirectional 0°, bidirectional 0-45°, and bidirectional 0-90° were compared. To better differentiate between the unidirectional and bidirectional print-methods, it would be enlightening to have a bidirectional 90° and bidirectional 0°, without the rotation in between layers. This would allow one to determine whether it is best to always allow the print-head to return to point "A" before continuing to deposit material once it reaches point "B" (i.e. unidirectional), or if it is better to allow the print-head to continuously deposit material while repeating the serpentine path from point "A" to "B" (i.e. bidirectional). Unidirectional 45° was never explored, nor unidirectional 0-90° nor unidirectional 0-45°.

All these possible combinations would allow for a much better design of experiment (DOE) to be conducted. The test could be conducted in the form of a full-factorial DOE that would readily allow for the creation of pareto charts representing which build-orientation options were the most statistically significant to each metric tested. Regression analysis could be performed to show the magnitude and direction of each build-orientation's effect on the various corrosion metrics.

Grain structure-microscopy would be helpful for each build-orientation to determine if the boundaries where different bead-paths of various print-directions intersect affect how likely corrosion is to propagate further into the sample. The fracture-site analysis performed in this experiment was relatively macroscopic and this analysis was unable to be performed due to time-constraints. Other existing research in additively manufactured steel parts showed significant focus on the importance of grain structures typically as a function of print-parameters. The interaction from one bead-path varying directions into another is not widely studied and is an opportunity for novel research in anisotropy.

Lastly would be the optimization of non-build-orientation print-parameters. This includes items such as the laser power, wire-feed rate, gas flowrate etc. One of the largest concerns with the samples analyzed was the presence of surface and internal defects such as pits, voids, and inclusions even before corrosion testing initiated. These defects often become the initiation-site for fracturing under tensile-load. If one desires to compare only the effects of the different build-orientations, it would be most beneficial to start with samples that do not include defects. By optimizing the print-parameters, these defects can be reduced or eliminated. This would result in the differences in performance from one sample to the next being more confidently attributed to the build-orientation rather than uncontrolled sample defects.

Bibliography

1) *Stainless Steel Chemical Composition Chart*. World Material. Retrieved July 28, 2024, from https://www.theworldmaterial.com/stainless-steel-chemical-composition/

2) *The Difference Between Austenitic and Ferritic Stainless Steel* (March 27, 2021). One Monroe. Retrieved July 28, 2024, from https://www.theworldmaterial.com/stainless-steel-chemical-composition/

3) ASTM (2024). *A240/A240M* (11). West Conshohocken, PA, USA: ASTM. Retrieved July 28, 2024 from https://www.htpipe.com/d/files/plate-material-grade/astm-a240.pdf

4) *Carbide Precipitation*. Hobart Brothers. Retrieved July 28, 2024, from https://www.hobartbrothers.com/resources/technical-guides/stainless-steel-technical-guide/carbide-precipitation/

5) Nicole (January 12, 2021). *316 vs 316L Stainless Steel: What's the Difference?* Bergsen Metals. Retrieved July 28, 2024, from https://www.theworldmaterial.com/stainless-steel-chemical-composition/

6) Brand, M., Moeini, G., & Marginean, G. (November 23, 2022). Corrosion behavior of 316L additively produced by Directed Energy Deposition-Arc. *Materials Today*, *78*. 242-250. https://doi.org/10.1016/j.matpr.2022.11.194

7) LibreText. *20.8: Corrosion*. Chem.LibreTexte.Org. Retrieved July 28, 2024 from https://chem.libretexts.org/Bookshelves/General_Chemistry/Map%3A_Chemistry_-_The_Central_Science_(Brown_et_al.)/20%3A_Electrochemistry/20.08%3A_Corrosion#:~:text=In%20contrast%20to%20these%20metals%2C%20when%20iron%20corrodes%2C,surface%20vulnerable%20to%20reaction%20with%20oxygen%20and%20water

8) Almubarak, A., Abuhaimed, W., & Almazrouee, A. (April 22, 2013). Corrosion Behavior of the Stressed Sensitized Austenitic Stainless Steels of High Nitrogen Content in Seawater. *International Journal of Electrochemistry*, *2013*(1). https://doi.org/10.1155/2013/970835

9) *Hydrogen Embrittlement* (2024). Hydrogen Tools. Retrieved July 28, 2024 from https://h2tools.org/bestpractices/hydrogen-embrittlement

10) Barrera, O., Bombac, D., Chen, Y., Daff, T. D., Galindo-Nava, E., Gong, P., Haley, D., Horton, R., Katzarov, I., Kermode, J. R., Liverani, C., Stopher, M., & Sweeney, F. (2018). Understanding and mitigating hydrogen embrittlement of steels: a review of experimental, modelling and design progress from atomistic to continuum. *Journal of materials science*, *53*(9), 6251–6290. https://doi.org/10.1007/s10853-017-1978-5

11) Ma, F.-Y. (2012). Corrosive Effects of Chlorides on Metals. *InTech*. https://doi.org/10.5772/32333

12) Haghdadi, N., Laleh, M., Moyle, M., & Primig, S. (August 26, 2020). Additive manufacturing of steels: a review of achievements and challenges. *Journal of Material Science, 56*. 64-107. https://doi.org/10.1007/s10853-020-05109-0

13) Özel, T., Shokri, H., & Loizeau, R. (February 8, 2023). A Review on Wire-Fed Directed Energy Deposition Based Metal Additive Manufacturing. *J. Manuf. Mater. Process, 7(1)*. https://doi.org/10.3390/jmmp7010045

14) Bernauer, C., Meinzinger, L., Zapata, A., Zhao, X.-F., Baehr, S., & Zaeh, M. F. (April 20, 2023). Design and Investigation of a Novel Local Shielding Gas Concept for Laser Metal Deposition with Coaxial Wire Feeding. *Applied Science, 13*(8). https://doi.org/10.3390/app13085121

15) Ribeiro, K. S. B., Mariani, F. E., & Coelho, R. T. (2020). A Study on Different Deposition Strategies in Direct Energy Deposition (DED) Processes. *Procedia Manufacturing, 48*. 663-670. https://doi.org/10.1016/j.promfg.2020.05.158

16) *VC-500A/5X AM HWD*. MazakUSA.com. Retrieved July 28, 2024 from https://www.mazakusa.com/machines/vc-500a-5x-am-hwd/

17) ASTM (2024). *E8/E8M* (13a). West Conshohocken, PA, USA: ASTM. Retrieved July 28, 2024 from https://www.galvanizeit.com/uploads/ASTM-E-8-yr-13.pdf

18) Shane (July 30, 2023). *Understanding Yield Strength: A Comprehensive Guide*. MachineMFG. Retrieved July 28, 2024 from https://www.machinemfg.com/yield-strength-guide/

Appendix

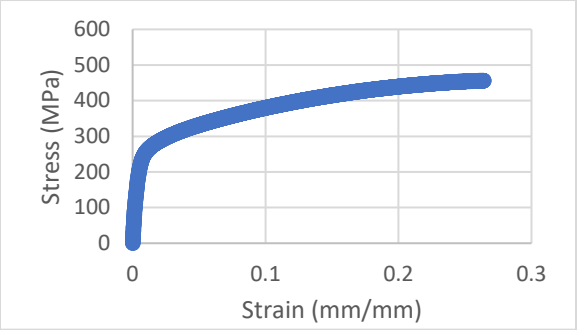

Figure 103: Stress-Strain Curve of Control Sample TA

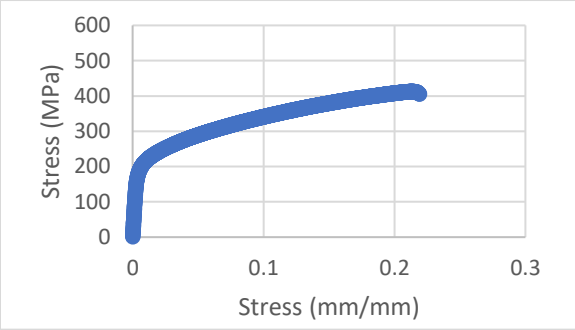

Figure 104: Stress-Strain Curve of 21-Day Sample 1A

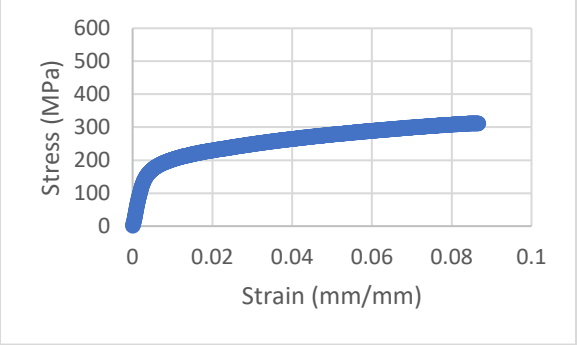

Figure 105: Stress-Strain Curve of 43.5 Day Sample 2A

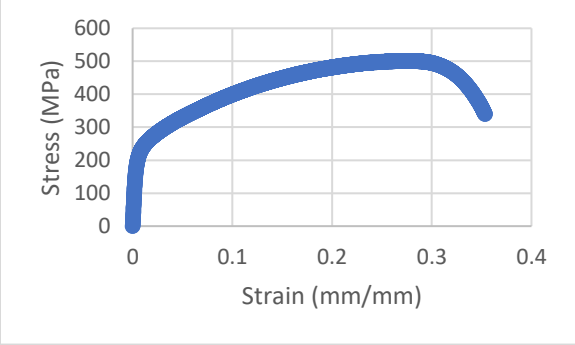

Figure 106: Stress-Strain Curve of Control Sample 3A

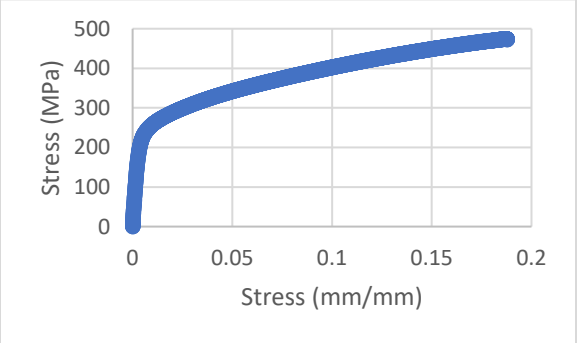

Figure 107: Stress-Strain Curve of 21-Day Sample 4A

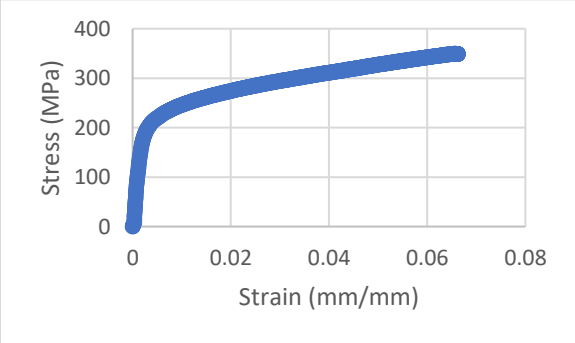

Figure 108: Stress-Strain Curve of 43.5-Day Sample 5A

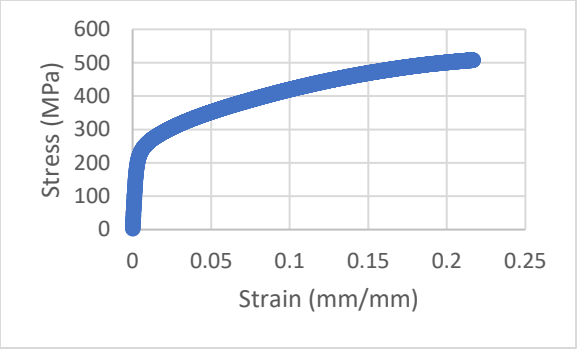

Figure 109: Stress-Strain Curve of Control Sample 6A

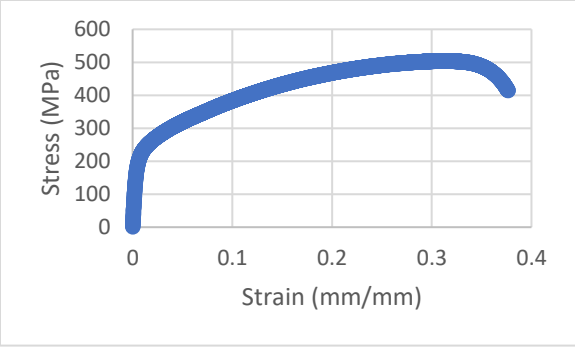

Figure 110: Stress-Strain Curve of Control Sample 7A

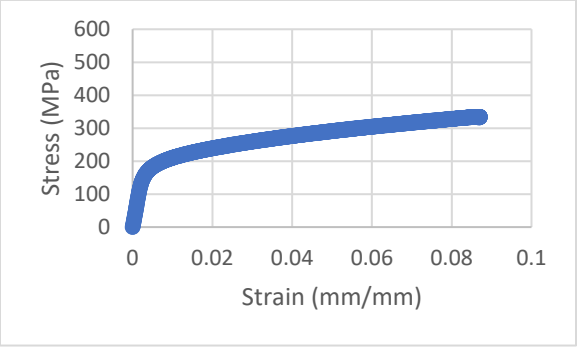

Figure 111: Stress-Strain Curve of 43.5-Day Sample 8A

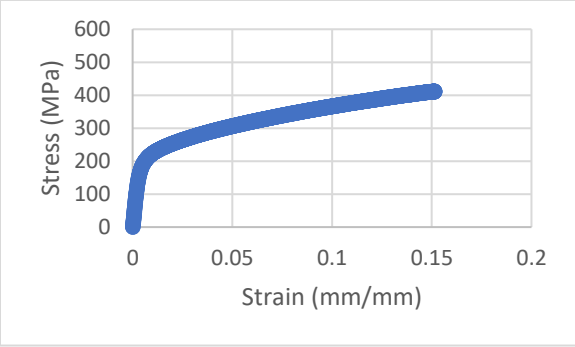

Figure 112: Stress-Strain Curve of 21-Day Sample 9A

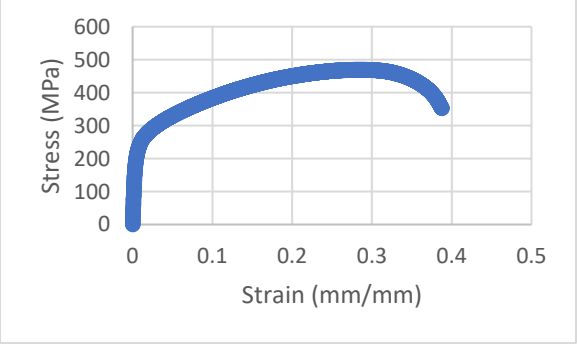

Figure 113: Stress-Strain Curve of Control Sample BA

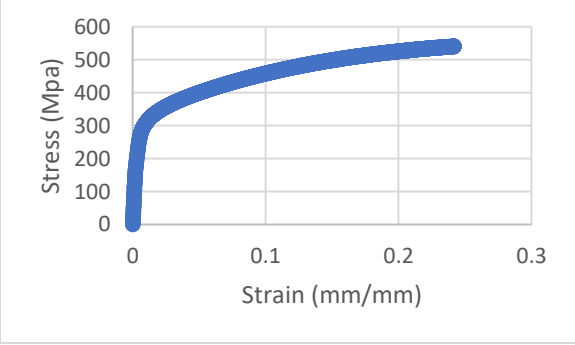

Figure 114: Stress-Strain Curve of 21-Day Sample 3B

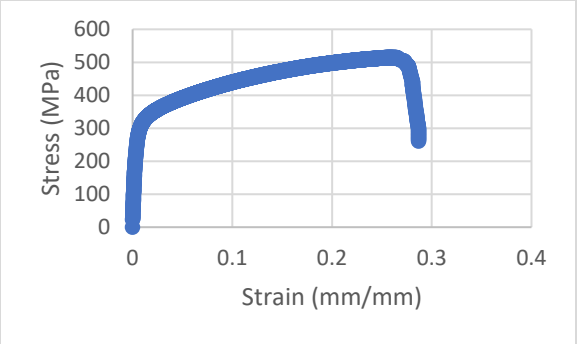

Figure 115: Stress-Strain Curve of 43.5-Day Sample 4B

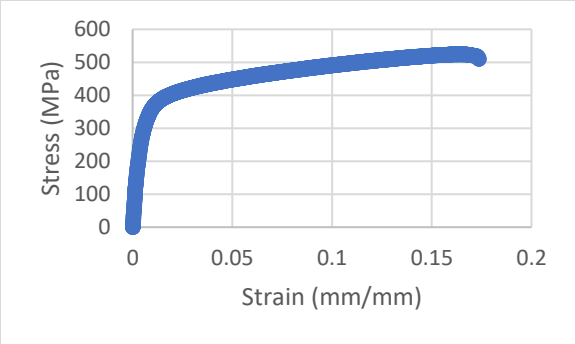

Figure 116: Stress-Strain Curve of Control Sample 5B

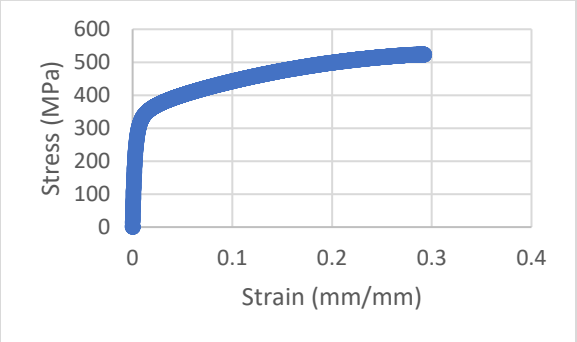

Figure 117: Stress-Strain Curve of 21-Day Sample 8B

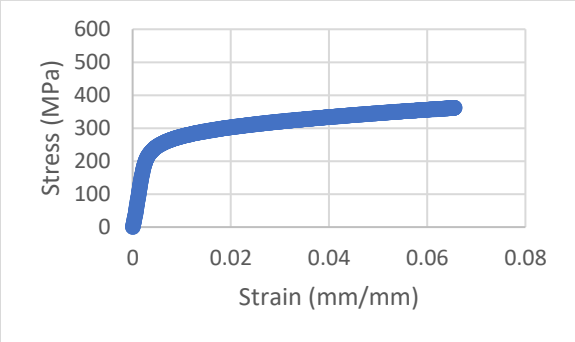

Figure 118: Stress-Strain Curve of 43.5-Day Sample 9B

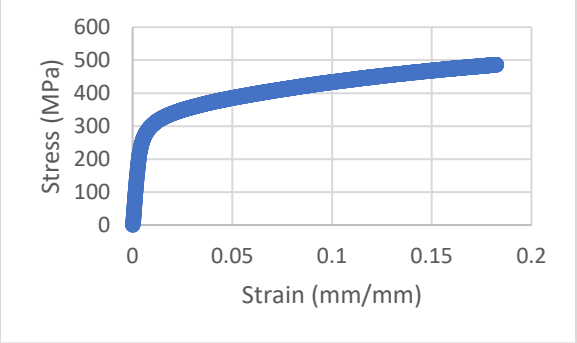

Figure 119: Stress-Strain Curve of Control Sample 10B

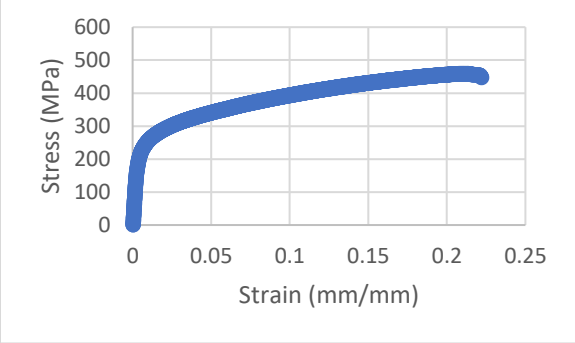

Figure 120: Stress-Strain Curve of 21-Day Sample 3C

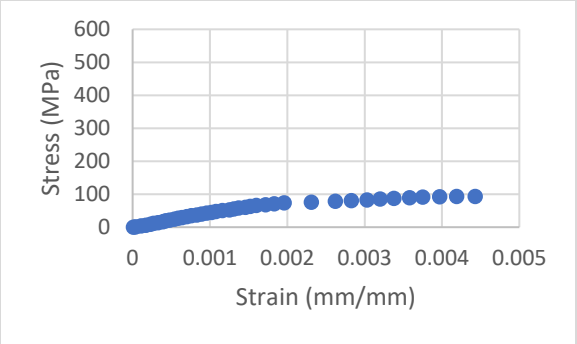

Figure 121: Stress-Strain Curve of 43.5-Day Sample 4C

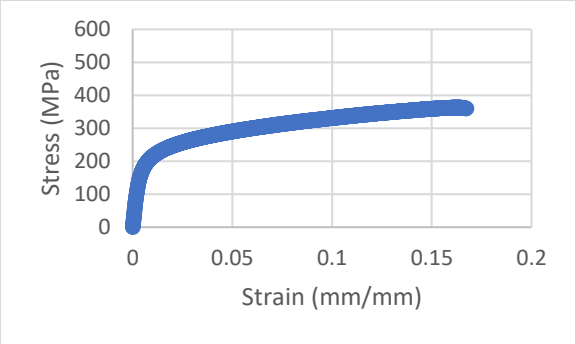

Figure 122: Stress-Strain Curve of 21-Day Sample 5C

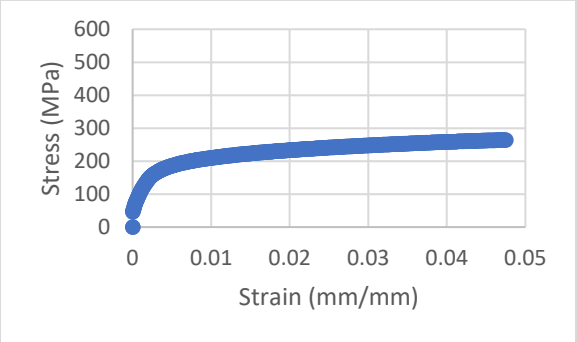

Figure 123: Stress-Strain Curve of 43.5-Day Sample 8C

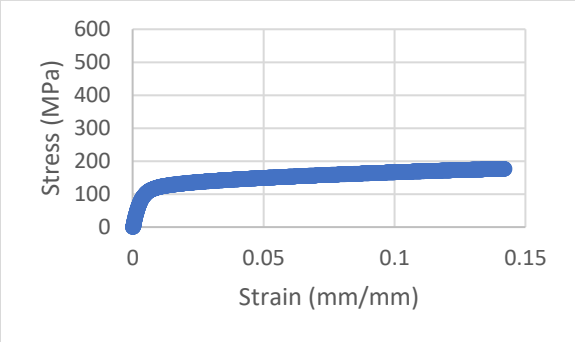

Figure 124: Stress-Strain Curve of Control Sample 11C

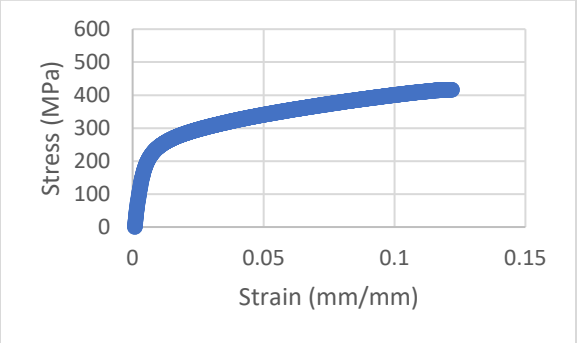

Figure 125: Stress-Strain Curve of Control Sample 1D

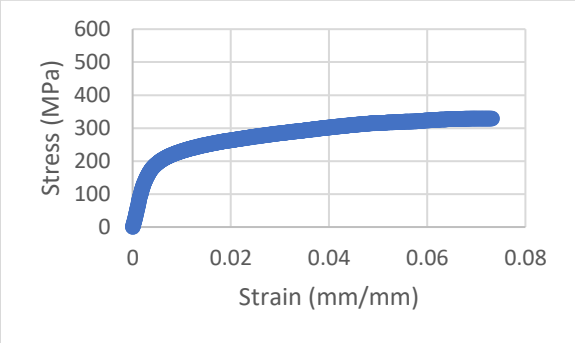

Figure 126: Stress-Strain Curve of 21-Day Sample 2D

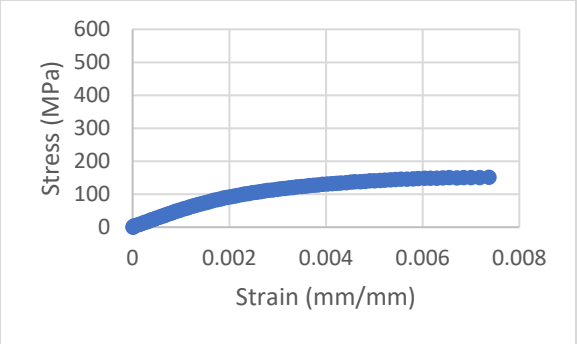

Figure 127: Stress-Strain Curve of 43.5-Day Sample 3D

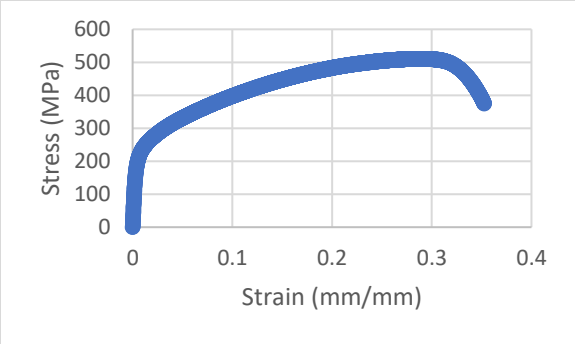

Figure 128: Stress-Strain Curve of Control Sample 4D

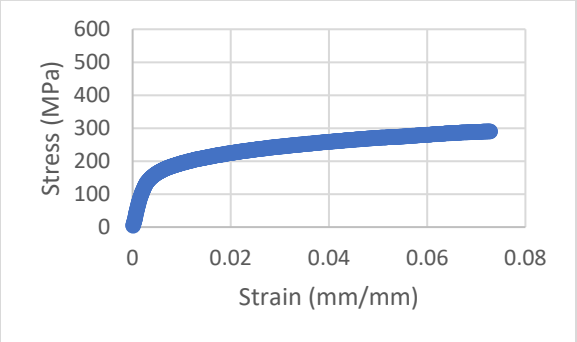

Figure 129: Stress-Strain Curve of 21-Day Sample 5D

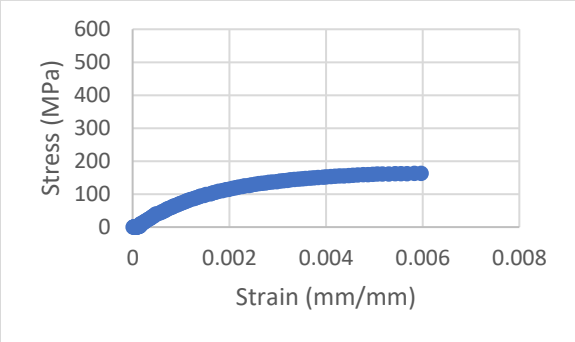

Figure 130: Stress-Strain Curve of 43.5-Day Sample 6D

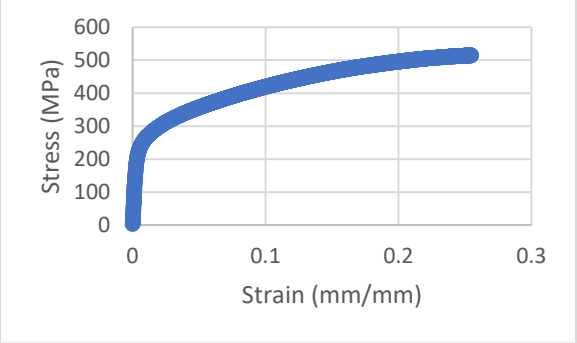

Figure 131: Stress-Strain Curve of Control Sample 7D

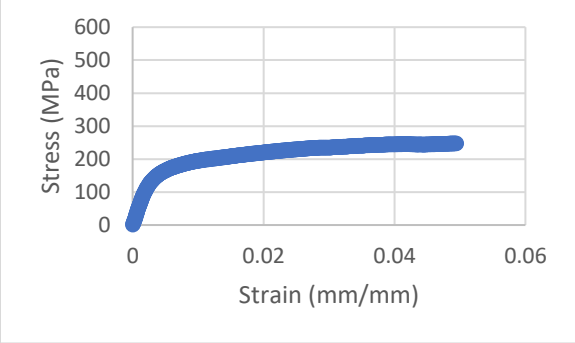

Figure 132: Stress-Strain Curve of 43.5-Day Sample 8D

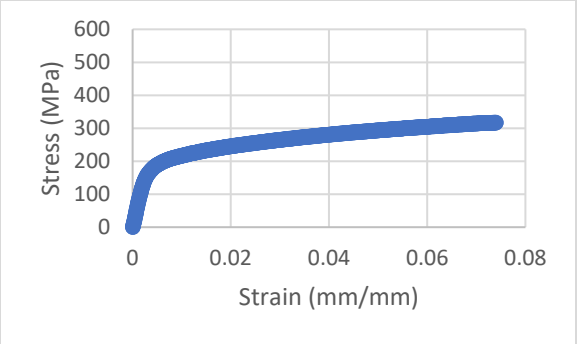

Figure 133: Stress-Strain Curve for 21-Day Sample 9D

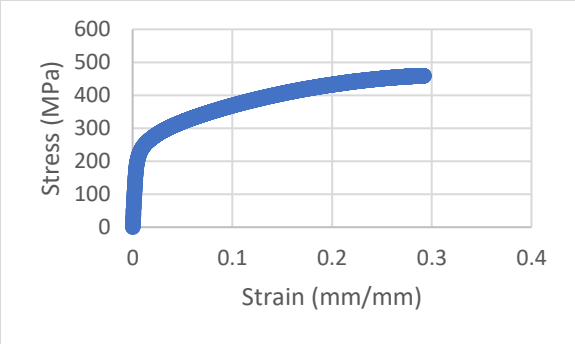

Figure 134: Stress-Strain Curve for Control Sample 10D

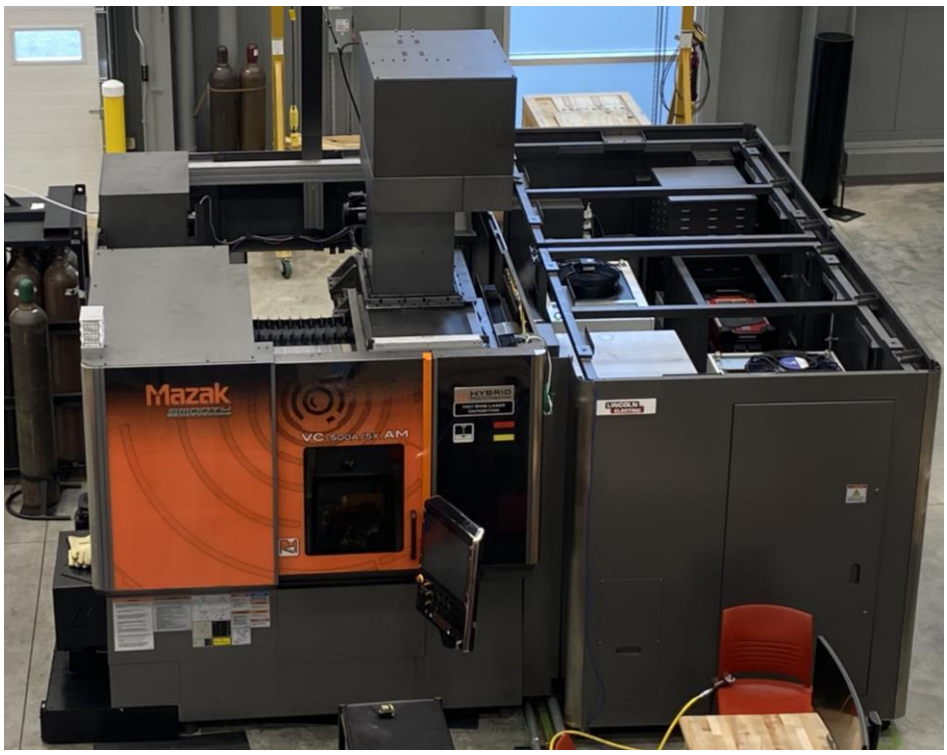

Figure 135: Mazak VC-500/5X AM HWD